Martian Ice Revealed by Modeling of Simple Terraced Crater Formation

E. Martellato[1,2*], A. M. Bramson[3,4], G. Cremonese[5], A. Lucchetti[5], F. Marzari[6], M. Massironi[7], C. Re[5], S. Byrne[3]

[1] Dipartimento di Scienze e Tecnologie, Università degli Studi di Napoli "Parthenope", Centro Direzionale Isola C4, 80143, Napoli, Italy

[2] Museum für Naturkunde, Leibniz-Institut für Evolutions- und Biodiversitätsforschung, Invalidenstraße 43, 10115 Berlin, Germany

[3] Lunar and Planetary Laboratory, University of Arizona, 1629 E University Blvd, Tucson, Arizona, USA

[4] Dept. of Earth, Atmospheric, and Planetary Sciences, Purdue University, 550 Stadium Mall Dr, West Lafayette, IN 47907, USA

[5] INAF-Osservatorio Astronomico di Padova, vic. Osservatorio 5, 35122, Padova, Italy

[6] Dipartimento di Fisica e Astronomia “Galileo Galilei”, Università degli Studi di Padova, via Marzolo 8, 35131, Padova, Italy

[7] Dipartimento di Geoscienze, Università degli Studi di Padova, via Gradenigo 6, I-35131 Padova, Italy

[*] Corresponding author. E-mail: elena.martellato@uniparthenope.it

Keywords: Mars, impact craters, ice, numerical modelling

Key Points:

- We performed numerical modelling to investigate the formation of simple craters with a concentric morphology on Mars
- The central pit dimensions are controlled both by the target material (damaged friction coefficient) and by the impactor (size and density)
- Our modeling shows water ice over basement bedrock can create wall terraces in simple craters

Abstract

Arcadia Planitia, a region in the northern mid-latitudes of Mars, displays an uncommonly high abundance of simple craters with a concentric morphology, which is indicative of layering beneath the surface. Radar measurements suggest that the near surface layers could be made of excess water ice. . In this study, we select two of these impact structures of similar size (D_c~500 m), model their formation through iSALE shock physics code, and investigate the dependence of the final crater morphology on the material model parameters (cohesion and friction coefficient).Our parameter study shows that the intact and damaged cohesion of the non-porous ice play a fundamental role to obtain a good fit between our models and the topographic profiles taken

from the Digital Terrain Models in terms of crater diameter, crater wall inclination, and depth and size of the upper terrace. The central pit shape is instead controlled by the damaged friction coefficient of the basaltic crust, but it is mainly affected by projectile density and speed. Our results confirm that two layers of relatively pure water ice, each with different rheology and porosity, can explain the unique double-terraced morphology of impact craters in Arcadia Planitia. The low values of cohesion we find for the ice might point to snowfall as emplacement mechanism in the region. The different thicknesses of the ice layers in the two crater areas seem to suggest variations in ice deposition and/or evolution history across Arcadia Planitia.

Plain-Language Summary

Impact craters are described by a bowl-shaped morphology at smaller sizes. Any departure from such a shape provides insight into subsurface target properties, including changes in density, strength, water content, porosity, composition, etc. In particular, the presence of steps (or "terraces") along the walls of simple craters provides a straightforward example of complexity within the planetary crusts, and indicates an abrupt transition from upper, weaker layers to deeper, stronger material. Using numerical modeling we studied two examples of terraced craters in Arcadia Planitia, Mars, to derive information about the rheological properties of the upper Martian crust. This analysis supports radar remote sensing measurements, and suggests shallow ice-rich layers in Martian mid-latitudes terrains could plausibly cause the terraces observed in these craters. The distribution and properties of water ice are important for understanding Mars' climatic history, as well as the availability of in-situ resources for future human exploration.

1. Introduction

Impact craters (or impact structures) are one of the most widespread landforms on planetary surfaces. Crater morphology naturally varies with size, showing either a bowl shape, or a flattened shape with central peak and terraced walls. The development of either of these morphologies depends on the extent of the collapse of the initial transient cavity, which is limited to crater rim and wall material slumping into the crater floor in the first case (simple craters). In the case of complex craters, modifications involve crater rise and rim collapse favored by the temporary strength weakening of the target material surrounding the transient cavity (e.g., Melosh, 1989). The impactor kinetic energy is not the unique controlling parameter for the final crater morphology, but also target properties such as layering, material strength, porosity, and thermal state can cause variation in the final crater morphology within a given crater class (e.g., Chandnani et al., 2019; Collins et al., 2008; Ivanov et al., 2010; Martellato et al., 2017; Osinski et al., 2019; Silber et al., 2017), due to differences in the propagation of the shock waves produced upon collision within the target medium (e.g., Melosh, 1989; Melosh & Ivanov, 1999).

The presence of a layered stratigraphy in planetary crusts revealed by crater morphology has been investigated by a number of authors. First laboratory experiments pointed out that an increase in the target material strength caused the modification of the canonical bowl shape of simple craters into central-mound, flat bottom, and concentric geometries for a decreasing thickness of the surficial weak layer over a stronger one (Oberbeck & Quaide, 1967). The relation between crater morphology and surficial layer thickness was then used to infer the thickness of the lunar regolith by means of morphometric measurements (e.g., Bart et al., 2011; Quaide & Oberbeck, 1968). From observational studies on Mars, Herrick & Hynek (2017) suggested similarly that the flat floors might develop in craters for the presence of a harder substratum placed at the base of the initial transient cavity. More recently, analogous investigations were carried out again as numerical experiments. Senft & Stewart (2007) showed that the shock impedance contrast between ice and rock layers could modify the crater

mechanics and produce changes in the final shape of the craters, as well as variation in the ejecta emplacement. Prieur et al. (2018) carried out systematic numerical simulations, showing that the progressive variation in the crater morphology is affected by impact velocity and the material strength of layers, whereas Martellato et al. (2017) investigated whether the inverse cone-truncated morphology of a lunar simple crater might be related to subsequent differently strengthened lava flow emplacement. At larger crater sizes, Hopkins et al. (2019) analyzed the effects of weak layers in a simulated planetary target by developing a new routine to improve computational resources when taking into account more realistic model setups. Other studies (e.g., Chandnani et al., 2019; Osinski et al., 2019) examined the effects of a layered stratigraphy on lunar craters in the transitional size range from the simple to the complex morphology (~15−20 km), and supported target layering as a key factor in explaining crater differences. Chandnani et al. (2019) found indeed that weak layers favor crater collapse, and the onset for the complex morphology occurs at a lower crater diameter in comparison to target with higher strength.

Lithological variations with depth have been identified as a natural attribute of planetary crusts (e.g., Collins et al., 2008; Hiesinger et al., 2001; Ono et al., 2009; Robinson et al., 2012; Senft & Stewart, 2007; Weider et al., 2010). A layered stratigraphy may also be expected on Mars. Barker & Bhattacharya (2018) illustrated the evolutionary sequence of the Northern plains since the Early Noachian era (cf. Figures 4 to 8 in Barker & Bhattacharya, 2018), with progressive diminishing of near surface water being due to environmental changes, including temperature and atmospheric pressure drop off. The thinning of the primordial ocean came in parallel with surface mantling of layers of Aeolian dust and volcanic ash, impact crater ejecta, volcanic flow emplacement, and fluvial sedimentation.

Throughout the Amazonian, the ice deposition and sublimation at different latitudes depends on climate variations, which in turn are primarily controlled by obliquity (e.g., Head et al., 2003). When Mars has been in high obliquity periods (>30°), ice at high latitudes is unstable and relocated to the equatorial regions. At the same time, the planet likely experiences high water vapor content in the atmosphere due to the higher insolation at the poles, and dust content in the atmosphere may rise due to strong winds. Periodically every ~40 kyr, Martian obliquity has decreased down to 22°−26°. In these conditions, ice in the polar areas is stable and re-accumulates, sublimating from the low- and mid-latitude regions. During sublimation of ice, impurities such as dust are left behind, leading to the formation of a porous surface “lag” deposit that can inhibit further sublimation (e.g., Head et al., 2003; Bramson et al., 2017). Therefore, the mid-latitude zone is characterized by a periodic sequence of ice deposition and ice removal, which may have built up a layered stratigraphy in the subsurface.

The depth and thickness of ice within the stratigraphy of the Martian surface, as well as its origin and mixture with lithic material and/or porosity, are still not completely characterized. Mellon et al. (2008), on the basis of measurements of Gamma Ray Spectrometer (GRS) onboard Mars Odyssey, suggested that much of the Martian mid- to high- latitudes is made up of an ice-rich permafrost layer, overlain by a thin layer of ice-free lag deposit that insulates the ice layer. At the latitudes of the Phoenix Lander (68°N), such ice table is expected to be few cm ($\lesssim 10\ cm$) under the surface, and in diffusive equilibrium with the water vapor present in the atmosphere (Mellon et al., 2008, 2009). The depth at which the ice material can be found is expected to increase with decreasing latitude, where temperatures are warmer and the ice is thus less stable. There is also abundant evidence for thick (tens of meters) ice deposits in the subsurface down to latitudes of ~35°, including sublimation-thermokarst geomorphologies (Dundas et al., 2015; Viola et al., 2015), thermal contraction polygons (Mangold, 2005; Mellon, 1997), visible evidence of ice-exposing new impact craters (Byrne et al., 2009; Dundas et al., 2014), and low dielectric constant estimates from radar subsurface measurements in Arcadia and Utopia Planitiae (Bramson et al., 2015; Stuurman et al., 2016).

In the northern mid-latitude Arcadia Planitia region, the morphological interface between an underlying basaltic crust and an upper weaker ice deposit may occur at a depth of tens meters based on the presence of reflectors in MRO Shallow Radar (SHARAD) data (Bramson et al., 2015), though the purity of the ice throughout the bulk

of the subsurface layer is debated (Campbell and Morgan, 2018). Dundas et al. (2018) discovered thick (~100 m) ice mantling deposits along scarps in the mid-latitude regions, including northern Arcadia Planitia. Bramson et al. (2017) modeled the conditions needed for the preservation of excess ice in the mid-latitudes within the last tens of millions of years. They suggested a bulk ice porosity of 25−35% and a dust content of 1−5% to fit the dielectric constants derived in the Bramson et al. (2015) and Stuurman et al. (2016) radar measurements. It is unclear how long porosity could be maintained in Martian ice deposits, though it should decrease with depth due to age and compaction from the overburden.

As snow/ice would be weaker than bedrock, crater morphologies (such as those described above) may be able to detect such ice mantling in mid-latitudes (e.g., proposed in Bramson et al. 2015). While previous studies had mapped intermediate-sized and large craters across Mars (≥5 km, e.g. Barlow et al,. 2017; Robbins & Hynek, 2012), Bramson et al. (2015) mapped the mid-latitude region of Arcadia Planitia (180°E–225°E and 38°N–50°N) (Figure 1) in CTX images (6 m/pixel) for simple craters with central pit/terraced wall morphologies, all of which had diameters of hundreds of meters. They found 187 craters with central pits in the crater floor, 35 of which have a second and shallower terrace along the crater walls. These two sets of impact structures, i.e. (i) craters with one terrace ending up in the central pit, and (ii) craters with a shallower and smaller terrace in addition to the deeper terrace where the central pit occurs, were classified by Bramson et al. (2015) as single- and double-terraced craters, respectively, and we retain the same nomenclature throughout this paper. Examples of single-terraced impact structures are Craters 4, 5, and 8 from Figure S3 (Supplemental material) of Bramson et al. (2015), while the other eight craters in their figure are examples of double-terraced craters. See also Table S1 from Bramson et al. (2015), and Table S1 in the Supplemental material of this manuscript for measurements of this selection of single- and double-terraced craters. The presence of two terraces suggests multiple strength contrasts in the subsurface across the region, and Bramson et al. (2015) found that the single-terraced craters are generally smaller than the double-terraced ones, and thus may not have been big enough to penetrate down to the strength contrast at the ice/bedrock interface.

The crater morphologies likely indicate a structural relation between terrace development and target properties. Indeed, as shown in laboratory experiments (e.g., Croft et al., 1979; Grey & Burchell, 2003; Lange & Ahrens, 1987), cratering efficiency is larger in icy targets than in rocky ones, due to shock impedance and contrast in the material strength. Similarly, Senft & Stewart (2008) investigated via modelling the effects of an icy layer with varying thickness and depth occurrence on the final morphology of impact craters, showing large variations in the excavation and modification phases due to the different shock propagation on icy and rocky material. These authors found that for a 1−2 km sized crater, the final structure has a single terrace (identified as inner crater by the authors) when the upper ice layer overlying the basaltic crust is sufficiently thick (≳200 m, case C in Figure 3 in Senft & Stewart, 2008), while it can develop a double terrace when upper stratigraphy consists of multiple layers (Figure 4 in Senft & Stewart, 2008).

In this study, we selected two double-terraced impact structures of the Bramson et al. (2015) database, and examined via numerical modelling whether an ice mantling scenario can explain the origin of the double terrace morphology observed in the impact structures of the Martian Arcadia Planitia region. As previously mentioned, we refer to such impact structures as "double-terraced craters" instead of "central pit craters", both for consistency with Bramson et al. (2015), and to make clearer the distinction between these “small” target-dependent structures and “large” central pit craters, whose formation mechanism may be more variegated. We will use the term “central pit” later in the text to indicate the small cavity in the center of the crater floor, and formed as a consequence of an impact on layered terrains. The paper is divided into three sections. We firstly describe the available data and observations of the selected terraced craters in the Arcadia Planitia region. The second section outlines the code used for the numerical modelling, and the initial conditions adopted for the two craters we analyzed. Finally, we present the results and discuss them in the general context of ice formation on Mars.

2. Observations

Arcadia Planitia is a volcanic region of Mars of Amazonian age. On its surface, it displays flow lobes, which are indicative of a basaltic composition of the bedrock (Greeley, 2013). The presence of other geomorphic landforms such as thermokarstically-expanded craters (Viola et al., 2015) and scalloped depressions (Dundas et al., 2015) are indicative of excess water ice (volumetric concentrations which exceed the pore space of the regolith) in the shallow subsurface, likely from the last 10s of Myr (Viola et al., 2015). Bramson et al. (2015) constrained the dielectric properties (and thus composition) of a decameters-thick layer in the subsurface by combining the delay times of a subsurface interface in SHARAD data with the depths to the bottom terraces measured in stereo pairs from the HiRISE camera (McEwen et al., 2010). They found an average bulk dielectric constant of 2.5 ± 0.28, concluding that the material in the upper decameters of the surface is excess ice of up to 75% volumetric fraction ice. SHARAD data cannot detect subsurface interfaces within 20−30 m of the surface, thus they were unable to detect a dielectric interface that may be expected to exist associated with a change in strengths necessary to explain the additional, shallower crater terracing (within ~25 m of the surface). Therefore, their results can only place constraints on the overall composition between the surface and bottom terrace, ignoring the finer structure that likely exists in the upper decameters of the subsurface, including the layering that causes the subtler upper wall terrace. This smaller, shallower terrace in the crater wall suggests additional complexity in the subsurface, perhaps a change in porosity or composition (such as a desiccated surface layer overlying ice). The fact that there are more than thirty craters with two terraces (which on average probe deeper than single-terraced craters) across Arcadia Planitia suggests that there are multiple layers within the subsurface throughout this region and that a similar subsurface structure likely extends across the study area.

Bramson et al. (2015) created eleven digital terrain models (DTMs) from HiRISE stereo pairs to determine the morphology and geometry of terraced craters within Arcadia Planitia. These impact structures are approximately 290−730 m in diameter, which places them in the simple morphology category. The pit diameter ranges from ~80 to ~340 m, while the pit-to-crater diameter ratio ranges between 0.14 and 0.55. The depth of the pit floor from the pre-impact surface can extend from ~25 m down to ~80 m. When measured from the lower terrace, it can vary between ~6 to 30 m, with a resulting pit depth-to-diameter ratio of 0.06−0.24. For this work, we took profiles across the DTMs of two of these craters (Figure 2). The two craters used for this study were chosen because they provided the clearest, most symmetric examples of the double-terraced morphology and exhibited wide, flat floor-level terraces at approximately the same depth. These two craters (craters labelled 0 and 2 from the supplementary material of Bramson et al., 2015) were also picked because they exhibited nearby (<15 km) subsurface reflectors in the SHARAD data, and thus contributed to the final dielectric analysis of Bramson et al. (2015).

Crater 1 (Figures 2a and c) is located at 46.58°N, 194.85°E (red star in Figure 1). It is ~710 m in diameter, and has a floor terrace (thought to be the ice-rock interface) at ~42 m depth with an additional, smaller wall-terrace at ~17 m depth. The pit is ~200 m in diameter, with a pit-to-crater diameter ratio of 0.28, and its bottom is at ~80 m below the Martian surface. The second crater we investigate here, Crater 2 (Figures 2b and d), is located at 47.94°N, 191.93°E (blue star in Figure 1), and has a diameter of ~590 m. Its shallower terrace is at 29 m depth, whereas the deeper, more prominent terrace is also placed at ~42 m below the surface. In this case, the pit is much smaller, approximately 50 m in diameter, with a pit-to-crater diameter ratio of 0.09, and its floor is at ~48 m below the surface. The pits of neither Crater 1 nor Crater 2 are rimmed, and the transition between the lower terrace and the pit is smooth, perhaps due to material slumping or post-impact erosion. The pit depth (measured from the lower terrace to its floor) is ~35 m and 7 m, respectively for Crater 1 and Crater 2. The pit depth-to-diameter ratio is 0.17 and 0.13, respectively for the two cases. Both craters have some asymmetry, possibly due to localized post-impact slumping of the walls as consequence of the impact obliquity. The central pits of both craters are elongated in one direction, in the east-west and southeast-northwest directions, respectively for the two craters, suggesting the direction of the impact (e.g., Örmo et al., 2013). Asymmetries in

the upper wall of Crater 2 (Figure 2d) have been also observed, consisting of an additional faint terrace, caused either by further complexity of the target or uneven slumping due to the impact geometry.

3. Numerical Modeling

3.1 Code description

The mechanics of crater formation is often studied through numerical modelling based on shock physics codes (Johnson & Anderson, 1987), which can model the propagation of shock waves through the equations of conservation of mass, momentum, and energy (the compressible Navier-Stokes equations). The behavior of matter is quantified by the Equations of State (EoS) and strength models, which describe the bulk thermodynamic material response and deviatoric deformations, respectively (e.g., Pierazzo et al., 2008).

To accomplish this study, we use the iSALE (impact Simplified Arbitrary Lagrangian Eulerian) shock physics code, in the Dellen version released on 6/7/2016 (Collins et al., 2016), which has been largely employed to study impact craters in planetary contexts (e.g., Collins et al., 2008; Martellato et al., 2017; Wünnemann et al., 2008). The present version represents the final output of a programming activity lasting about thirty years (and still in development), during which the original SALE hydrocode (Amsden et al., 1980) was modified from a code simulating single-material Newtonian-fluid flow to a code simulating dynamic processes like impact cratering with a higher degree of realism to account for the propagation of shock waves and the behaviors of geologic materials when subjected to quick variations of pressures and temperatures. The most important enhancements include, but are not limited to, an elasto-plastic constitutive model, multiple rheologies, different kinds of equations of state (e.g., Tillotson EoS or ANEOS), a damage model, the $\varepsilon-\alpha$ porosity compaction model, and the Acoustic Fluidization model for simulating the collapse of large craters (Collins et al., 2004, 2011; Ivanov et al., 1997; Melosh et al., 1992; Wünnemann et al., 2003, 2006). iSALE was validated against laboratory experiments at low and high strain-rates (Wünnemann et al., 2006), and other shock physics codes (Pierazzo et al., 2008), in order to favor a more genuine interpretation of the studied phenomena from the models.

3.2 Projectile outline

The projectile is simplified to a homogeneous sphere with basaltic composition, hitting the Martian surface perpendicularly. A number of previous works (e.g., Cremonese et al., 2012; Davison et al., 2010, 2012) used dunite to approximate the Main Belt asteroids, due to the larger percentage of small bodies classified as ordinary chondrite (e.g., Binzel et al., 2003). However, we use instead a basaltic composition for the projectile, to follow the approach of reducing the number of materials in the models, and thus to reduce the computational time costs, similarly to previous numerical investigations (e.g., Pierazzo et al., 2005; Senft & Stewart, 2008). Having used the same material for crust, the projectile has a porosity of 10% (cf. section 3.5 for the porosity description) and a density is ~2500 kg/m^3, , which might well approximate C-type asteroids, the most common class in the Main Belt (e.g., Consolomagno et al., 2008). Porosities lower than 10% are expected for ordinary chondrites, while carbonaceous chondrites usually have porosities higher than 20% (Consolomagno et al., 2008). Britt et al. (2002) found 11%, with a 1σ spread of ±5%, as average porosity among the various meteorite types. Therefore, we believe that the adopted value of 10% can represent a good compromise for our models.

The two projectiles have different sizes (20 m and 15 m, respectively for Crater 1 and Crater 2; cf. Table 1), to account for the different crater diameter, but are defined by the same number of grid cells (16 cppr (cell per projectile radius)), in order to obtain comparable results. The assumption of vertical impact is required due to the 2D nature of iSALE, which contrasts with studies that show oblique impacts as favorable pathway of impacting objects (e.g., Melosh, 1989; Shoemaker, 1962). For the two studied impact structures, the obliquity

of the impact is suggested by local asymmetries in the observed morphology. Therefore, we configure a more realistic setup by using as impact velocity the vertical component of the speed vector expected from the velocity distribution (e.g., Bland & Smith, 2000; Bottke et al., 1994; Davis, 1993; Flynn & McKay, 1990; JeongAhn & Malhotra, 2015). Employing 10.2 km/s as mean impact velocity, its vertical component at an impact angle of 45° corresponds to ~7 km/s.

3.3 Target outline

We simulate the formation of the two double-terraced craters in an Eulerian mesh, where materials move through the numerical cells that are fixed in space. The grid spacing consists of a high-resolution zone covering the impact area surrounded by a zone of progressively lower resolution, where the cell size increases by a factor of 1.05 from the previous cell, which prevented spurious shock wave reflections at the target boundaries. The total grid is slightly different for the two impact structures, being 2360 m × 3120 m and 2353 m × 3116 m in radial distance from the impact center and vertical extension, respectively for Crater 1 and Crater 2. The high resolution zone is 560 m × 520 m and 553 m × 512 m, respectively for the two craters. In order to reduce the computational time, we ran the preliminary test simulations verifying projectile dimension and the formation of the double-terraced morphology at the lower resolution of 10 cppr. The results presented here are then obtained by running specific models at the higher resolution of 16 cppr, which implies a cell size of 1.25 m and 0.9375 m, respectively for Crater 1 and Crater 2 (see Table 1 for the best fit model values, and later in the text and in the Supplemental material for the model value ranges showed in the present study).

The target is approximated by three layers, as shown in Figure 3, in order to test hypotheses that the development of the lower terrace and the central pit is due to the transition from a layer of subsurface ice to a low-porosity rocky crust. In both studied craters, this interface occurs at a depth as great as ~40 m. The ice stack is further sub-divided into a porous and non-porous ice component, to take into account the presence of the subtle upper terrace. Indeed, the shallower terrace being less defined with respect to the deeper terrace may suggest more similarities within the these two ice layers, like a change in porosity rather than either material and/or strength differences (Bramson et al., 2015). This ice deposit is expected to be covered in turn by a layer of dust less than ~1−2 meters at these latitudes (Bramson et al., 2017; Byrne et al., 2009; Dundas et al., 2014, 2018) that inhibits the sublimation of ice material. However, such a regolith layer is not included in our simulations because it would be barely resolved by the model resolution and thus not have a large effect on crater outcome.

The basement is assumed to be of basaltic composition, justified by the early work of Greeley & Spudis (1981), who suggested that 70% of the crust was resurfaced by basaltic volcanism. More recently, a basaltic composition has been documented by several spectroscopic studies in situ (e.g., Grotzinger et al., 2005), or by geological investigations of the Martian surface (e.g., Andrews-Hanna et al., 2010), and elemental composition and petrological measurements of Martian meteorites (e.g., Baratoux et al., 2014; McSween et al., 2009). All these analyses agree that the Martian crust is mainly composed of basalts, whereas siliceous, carbonate, quarzitic and sulphate rocks are underrepresented. Basalt was used as representative of the Martian crust also by a number of previous modelling investigations (e.g., Ivanov & Pierazzo, 2011; Ivanov et al., 2010; Pierazzo et al., 2005; Senft & Stewart, 2008; Watters et al., 2017). Ice material was tested and implemented in numerical investigations to describe the surface of a number of planetary bodies, including Ganymede, Europa, and Mars itself (e.g., Bray et al., 2008, 2014; Senft & Stewart, 2008; Silber & Johnson, 2017).

The thermodynamic behavior of basalt is given by the ANalytical Equation Of State (ANEOS) (Thompson, 1970; Thompson & Lauson, 1972), whereas the behavior of ice by the Tillotson EoS (O'Keefe & Ahrens, 1982; Tillotson, 1962). Although the Tillotson EoS does not allow to model state transitions as melting and vaporization during the initial stages of the impact process, our study is focused on the final crater morphology, providing justification for our use of a simpler EoS.

The temperature is set to the constant value of 180 K within all target (cf. Supplemental Material for temperature influence on crater morphology). We choose a thermal gradient of 15 K/km, according to other previous impact modelling studies on Mars (e.g., Ivanov & Pierazzo, 2011; Pierazzo et al., 2005), where the surface was modeled as a mixture of rock and ice. The thermal gradient value is based on Clifford (1993)'s estimates, and is expected to have only a very poor influence in a ~300 m thick target.

3.4 Strength Models for Basalt and Ice

The rheology of ice representing the porous ice layer is described by the Drucker-Prager model (e.g., Drucker & Prager, 1952), which predicts a linear dependence of the shear strength Y on pressure P:

$$Y = Y_0 + \mu_d P \qquad \text{(Eq. 1)}$$

where Y_0 is the cohesive strength at zero pressure and μ_d the coefficient of internal friction. For the cohesion Y_0, we test the values between 1 kPa and 10 kPa, whereas for μ_d we consider the values between 0.18 and 0.6, values belonging to the range obtained from laboratory and field data by Haehnel & Shoop (2004) and Lee & Huang (2014).

The intermediate non-porous icy layer is described by a pressure and damage-dependent strength model that considers rock failure (Collins et al., 2004). The strength Y is calculated as (Ivanov et al., 1997):

$$Y = (1 - D)Y_i + DY_d \qquad \text{(Eq. 2)}$$

in order to take into account the deformational history during crater formation. In Equation 2, Y_i and Y_d are the static strength of the intact and damaged material, respectively, and D is the damage which can vary between 0 and 1. We follow the approach of Bray et al. (2008, 2014), who adopted the Lundborg (1968) criterion to describe the behavior of both intact and damaged ice. Therefore, the intact and damaged strength equations assume the following formulation:

$$Y_i = Y_{i0} + \frac{\mu_i P}{1+\mu_i P/(Y_M - Y_{i0})} \qquad \text{(Eq. 3a)}$$

$$Y_d = Y_{d0} + \frac{\mu_d P}{1+\mu_d P/(Y_M - Y_{d0})} \qquad \text{(Eq. 3b)}$$

where Y_{i0} is the shear strength at zero pressure (cohesion of the intact material at zero pressure), μ_i is the coefficient of internal friction, and Y_M is the von Mises plastic limit of the material, Y_{d0} is the effective cohesion of the damaged material, and μ_d is the coefficient of friction at low pressure.

On the basis of a number of laboratory experiments (e.g., Arakawa & Maeno, 1997; Arakawa & Tomizuka, 2004; Beeman et al., 1988; Croft et al., 1979; Durham et al., 1983; Hiraoka et al., 2008; Jones, 1982; Petrovic, 2003), compressive strength is found to vary between 5 MPa and 25 MPa. However, the measured values are sensitive to a lot of factors, including confinement (e.g., Jones, 1982; Weiss & Schulson, 1995), strain rates (e.g., Arakawa & Maeno, 1997), temperature (e.g., Schulson, 2001), and salt or rock-mixture (e.g., Hiraoka et al., 2008; Schulson, 2001). For example, Schulson (2001) reviewed brittle failure of ice in different temperature conditions, and for the uniaxial brittle compressive strength observed a variation from ~2 MPa to 12 MPa, for a decrease in temperature from 272 K to 230 K. At a temperature of 230 K, the water ice is stronger by a factor of two than the saline ice (Schulson, 2001, and references within). On the other hand, Durham and Stern (2001) observed that in planetary contexts intact ice is hard to find, but it may exist as pre-faulted (in brittle regime, this is referred to pre-existing planes of weakness developed as shear fractures, e.g., Jaeger et al., 2007). In our simulations, we test the value of 10 MPa for the intact strength Y_{i0}, but lower values are also taken into account (see the results and discussion sections). The intact coefficient of friction μ_i is set to 2.0 (Beeman et al., 1988). We vary the damaged cohesion Y_{d0} between 0 kPa (from Senft & Stewart, 2008) and 0.5 MPa (from Bray et al.,

2014). Based on laboratory experiments (Beeman et al., 1988; Durham & Stern, 2001), the damaged coefficient of friction μ_d is found to vary between 0.2 and 0.55, but its value is affected by temperature too (Schulson, 1990). In our models, we test the values for the friction coefficient between 0.18 and 0.6.

The basaltic crust is also described by Equation 2, while the intact strength is represented by the Lundborg (1968) approximation (Equation 3a), and the damaged strength accounts for frictional forces between the fragments, as represented by the Coulomb dry-friction model given in Eq. (1). The values for the basalt are taken from a numerical investigation of a Martian large basin by Ivanov et al. (2010), except the damaged friction coefficient μ_d, for which we assumed a higher value (0.8 instead 0.6), similarly to the approach of Vasconcelos et al. (2019) and Senft & Stewart (2008).

Like in previous numerical investigations of small craters (e.g., Martellato et al., 2017), we do not implement the acoustic fluidization model (Melosh, 1979). Acoustic fluidization provides a rheological model to explain the temporary weakening of target material during the collapse of large complex craters (Melosh & Ivanov, 1999; Wünnemann & Ivanov, 2003). Silber et al. (2017) found that acoustic fluidization can affect also simple impact structures, but its influence becomes less important with increasing diameter. Their numerical models showed a variation of 3% and 7%, respectively in the diameter and depth values, by varying the acoustic fluidization parameters at a crater size half the threshold of the simple-to-complex transition. In the present studied cases, the craters are approximately one tenth the dimension expected for the simple-to-complex transition (~10 km), and this might ensure the negligible effect of the acoustic fluidization on the final outcome.

3.5 Porosity

In our modeling, the ice layers are not only characterized by a different rheology, but also by a different porosity. Bramson et al. (2015) proposed that the bulk dielectric constant of Arcadia Planitia could be as low as 2.5, which is less than the value of pure water ice (3.15; Ulaby et al., 1986). It is thus plausible that porosity may contribute to the multi-layer stratigraphy, and the development of the upper terrace along the crater walls. To test if porosity contrasts and layering within an ice deposit could generate the double-terraced craters in Arcadia Planitia, we set 35% as the porosity of the shallower ice layer over a non-porous ice layer.

Porosity is also set in the basaltic crust. Early studies suggested that the Martian crust might be analogous to the lunar crust, since it developed from a similar initial period of intense asteroidal bombardment that caused the formation of blocky porous megaregolith (e.g., Hartmann, 1973), justifying use of the porosity estimates on the Moon also in the Martian context. Recent remote sensing measurements of the Gravity Recovery and Interior Laboratory (GRAIL, e.g., Zuber et al., 2013) mission indicated that the porosity of the lunar upper crust may reach 20%, with an average value of 12% (Wieczorek et al., 2013). Goossens et al. (2017) combined gravity and topography data similarly, deriving a porosity between 10% and 23%. A porosity value of 10−20% was also found for the upper 10-km of the Martian surface by MacKinnon & Tanaka (1989) on the basis of theoretical and experimental measurements. The porosity of the near subsurface can be additionally estimated from the Martian meteorites. Coulson et al. (2007) found that the porosities of the studied Martian meteorites are lower than the porosity of 12% measured on basalt from Mt. Etna. Macke et al. (2016) measured a porosity as high as 18% only for one sample (chassignite, NWA 2737), and values between 5% and 10% for all the other studied cases. Hence, consistent with other numerical studies (Jones et al., 2011), we adopt 10% as the porosity of the Martian crust, but, being higher values of porosity suggested for the upper Martian crust (e.g., Goossens et al., 2017; MacKinnon & Tanaka, 1989), we also carry out several tests with a 20% porosity (shown in the Supplemental material).

In iSALE, porosity is described by the ε-α porosity model developed by Wünnemann et al. (2006), and refined by Collins et al. (2011), which accounts for the collapse of pore space through a compaction function that depends upon volumetric strain. Porosity in craters wall and floor can grow under the effect of dilatancy. Few

investigations are available so far to show how crater morphology is affected by dilatancy (e.g., Artemieva et al., 2004; Collins, 2014; O'Keefe et al., 2001). In this study, we do not implement the dilatancy model, but we test it only for a couple of runs to evaluate its effect on the crater shape (shown in the Supplemental material). We use the values derived by Collins (2014).

3.6 Comparison to Observations

The best fit models for the two double-terraced impact structures are derived by comparing the outcomes of the numerical simulations with the craters' DTMs. The grid of the numerical simulations assumes an elevation of zero at the top of the pre-impact surface. We use the pre-impact surface of the numerical grid as zero of the reference elevation for the observed crater profiles too, and so we shift the DTM data along the vertical direction of a quantity equal to the average elevation of the area immediately surrounding the craters.

The profiles of both craters present some asymmetries, which likely arose from the obliquity of the impact and inhomogeneity in the target, including possible inclines of the Martian surface at the crater sites. Therefore, to test our models, we use a representative profile obtained by averaging four perpendicular segments of elevation data taken between the center of the crater and its rim. To compute the DTM error, we follow the approach of Martellato et al. (2017), and take the maximum semi-dispersion, due to the low number of crater elevations used to derive the representative profile. The upper and lower wall inclinations are derived as the inverse tangent function of the line approximating the crater walls, by using the formula: $\alpha = \tanh^{-1}\left({}^{\Delta y}/_{\Delta x}\right)$, where Δx and Δy are the interval along the radial and the vertical direction of two points along each section of the wall. The related uncertainty is computed through the error propagation. It is based on the squared root of the sum of the squares of the partial derivatives of $\alpha(\Delta x, \Delta y)$ with respect to Δx and Δy (cf. Supplemental Material). Being a synthetic profile, we use twice the space resolution as uncertainties of Δx and Δy.

The comparison between the simulated and observed craters is conducted by correlating specific features of the impact structures, and specifically the diameter D_c, rim R_c, and depth d_c of the crater, the diameter D_{pit}, depth d_{pit}, and rim R_{pit} of the central pit, and the size $\boldsymbol{\Delta}$, depth d, and inclination $\boldsymbol{\alpha}$ of the upper (with the subscript 'UT') and lower (with the subscript 'LT') terraces. Crater and pit diameters of the observed and modeled impact structures are measured from rim to rim. Differently to other works of literature (i.e., Silber & Johnson, 2017; Watters et al., 2015), depths of both observed and modeled craters are measured from the zero-level surface, since we would like to make a direct relation between crater features and target stratigraphy. In the case of the modeled crater, it is given by the pre-impact surface setup in the numerical grid. In the case of the DTM profile, it is given by the mean regional topography, since, as explained above, the reference profiles were synthetized to remove local asymmetries, including variations in the elevation of the Martian terrains surrounding the two craters. The depth of the central pit is measured from the lower terrace. Rims are measured from the nearest lower surface, corresponding to the pre-impact surface in case of the crater rims, while in the case of the pit rim it is the lower terrace. In this regard, we note that the observed pit rim has a "negative" value, because as explained in Section 2, the central pit is rimless due to slumping or post-impact erosion. To derive the upper and lower wall inclinations of the modeled craters and their error, we follow the same approach used to compute wall inclinations on the DTM profiles. In this case, we take twice the resolution of the cell as uncertainties of Δx and Δy.

The error in the measurements was computed following the approach of Silber & Johnson (2017). The uncertainty of the crater radius is the difference between the values of the crater radius measured at the rim and at the pre-impact surface, divided by four (cf. Figure 3, and Figure 5 in Silber & Johnson, 2017). The crater diameter error is then the double of this value. Similarly, the uncertainty of the pit radius is the difference between the values of the pit radius measured at the pit rim and at the lower terrace, divided by four (cf. Figure 3). The pit diameter error is then the double of this value. The uncertainties in the crater and pit depths, as well

as the terrace widths, are taken as double the cell size (i.e., 2.5 m and 1.9 m, respectively for Crater 1 and Crater 2). Since terraces may present a faint inclination, the depth of the upper wall terrace represents the average values measured at its extreme. In the case of the lower terrace, where the pit rim could erroneously perturb the final value, we take as depth the elevation measured in the middle point of the terrace. The uncertainty in the terrace depths is instead computed as the maximum semi-dispersion of the depth values measured at the extreme of the terrace. Finally, the uncertainties in the upper and lower wall inclinations are computed through the error propagation, as shown above.

4. Results

First, numerical simulations, with material parameters used in previous studies (Bray et al., 2008; Ivanov et al., 2010), were run at a lower resolution (10 cppr), to determine the best-fit projectile size for each crater whilst keeping the simulation duration to a reasonable time. A preliminary crude estimation of the projectile dimensions was derived via scaling laws (Schmidt & Housen, 1987). The impact speed is kept constant to 7 km/s through overall this analysis. Several simulations are run at a lower velocity, and will be discussed in the Supplemental material. We vary both projectile dimensions and material model parameters including intact and damaged cohesions, and damaged friction coefficient of the layers, in order to fit numerical models with the observed nested-crater morphology. The projectile density is instead kept constant for all the simulations, except one simulation where we used a cometary-like impactor. The projectile dimensions are tuned to primarily fit the crater diameter, whereas the material parameters to fit the crater inner features (e.g., wall slope, depth and width of the upper and lower terraces, etc.). Given the projectile size, the final crater diameter can have variability lower than 25% when varying material parameters. Hence, we keep this value as uncertainty on the final projectile dimensions. For the assumed impactor density and velocity, we find that Crater 1 requires a projectile radius of 20 m, whereas Crater 2 forms from a smaller projectile, with radius of 15 m. The same strength parameters are adopted for both craters, because we additionally aim at evaluating which effects on the cratering process and the final crater shape would be associated to a different thickness of the porous ice layer. Indeed, while the basalt crust is at the same depth of ~42 m, the interface between the porous and non-porous ice layer is at 15 m and 29 m, respectively in the two cases. Lastly, a selection of models is run at the higher resolution of 16 cppr, and is discussed in the following paragraphs separately for Crater 1 (section 4.1) and Crater 2 (section 4.2). All the models shown in the following sections are run until the craters are completely developed. This means that the transient cavity is modified by gravity to reach its angle of repose, and the ejecta is deposited on the surrounding region (e.g., Melosh, 1989). This corresponds to a simulated end time of 25 s.

In Figure 4, time series snapshots of the formation of Crater 1 (left) and Crater 2 (right) are shown for the best fit model (whose parameters are reported in Table 1). In the Supplemental material, a movie of crater formation is also provided. The color map is referred to the three different target materials (porous ice, non-porous ice, and crust). The best fit model is obtained by adopting an effective damaged cohesion Y_d equal to 0.2 MPa for the basalt basement, and 10 kPa for both porous and non-porous icy layers. The intact cohesion Y_i of the non-porous ice layer is set to 50 kPa, a value which might indicate either compacted snowfall which has not fully sintered or impact fracturing (see Supplemental material for more details).

As the shock wave that originates upon collision propagates away from the impact site, it decreases in intensity, while the residual velocities contribute to the excavation and displacement of the target material (Figure 4b). The contrast between the shallower layers of low cohesion ice material and the deeper basaltic crust causes differentiation in the particle velocity field, and therefore in the excavation flow (e.g., Lange & Ahrens, 1987, Senft & Stewart, 2008). In turn, this causes the cavity to grow independently in the two regions, and the ejecta of the ice strata to be separately launched from the ejecta of the basement layer. As observed also by Senft & Stewart (2008), when the crater diameter is at least ten times the thickness of the upper weaker layer, the

decoupled motion of the two regions gives origin to a concentric morphology. The crater dimensions are modulated by the rheology of the porous and non-porous ice layers, whereas in the lower basaltic crust a nested inner cavity (corresponding to the central pit) develops.

As the crater grows, the target material is ejected towards the surrounding surface (Figure 4c), while the rocky ejecta originates from the inner smaller crater is embedded into the non-porous ice layer. At the same time, the gravity-driven collapse causes the different materials to slump differently until the crater reaches its stable configuration (Figure 4d): the icy material begins to slump towards the cavity center in a fluid manner (due to the low cohesion Y_d (10 kPa) and the low coefficient of friction μ_d (0.18)), but without experiencing melting. The target material would undergo melting after it is reached the specific pressure for phase transitions (2.9 GPa for ice in a Martian-like environment with a surface temperature of 200 K and atmospheric pressure of 6 mbar, e.g., Senft & Stewart, 2008). Pierazzo et al. (1997) showed that the center of the melted region differs from the one of the isobaric core. In addition, the depth and extent of the melted region depends on the impact velocity (e.g., Pierazzo et al., 1997). According to least-squares fit of numerical simulation outputs on ice, the melted region should be centred at a depth of about 2.2 times the projectile radius, from where it extends up to about 2.8 times projectile radii (cf. Table II in Pierazzo et al. 1997). In the basaltic crust, where most of the impact energy is released (cf. section 5.4), the central pit develops without undergoing breccia infilling. This material emplacement is expected in simple craters, where the lens thickness can be as much as half the initial transient cavity depth.

4.1 Crater 1.

Table S2 in the Supplemental material summarizes the numerical values of the features of Crater 1 for all the models discussed in this section. The measurements of the crater features and their errors are computed as described in Section 3.6 (cf. also Figure 3). In Figure 5, we report the last snapshot (at t=25 s) for Crater 1 in the case of the best fit model. From this output, we see that the modeled central pit is 1.05 times larger, and 1.7 times deeper than the observed one. In addition, it is rimmed, with a rim height of 1.6 m from the lower terrace (the reference surface for the pit), which cannot be accounted for the model uncertainty of 2.5 m: the observed central pit has a smooth and eroded profile, and the point of its maximum radial extension has an elevation of 2.3 m below the reference elevation given by the lower terrace. The width of the upper and lower terraces deviates ~3% and ~13%, respectively. The inclination of the upper and lower walls of the modeled crater is smaller by ~11% and 0.3% than the DTM ones, respectively.

In order to both find the best fit model and investigate the dependence of the crater morphology on the parameters of materials included in a multilayered stratigraphy, we vary the intact and damaged cohesions, and the damaged friction coefficient. The implementation of half of the intact cohesion Y_i in the deeper basaltic crust (compared in Figure 6a and 6b) produces no large difference in the final result, except the central pit sizes (the halved Y_i model caused the pit diameter to be 1.3 times larger and 2 times deeper than the observed crater profile). A variation of four orders of magnitude of the intact cohesion Y_i for the non-porous ice layer is shown in Figures 6c to 6e. The higher value (10 MPa, Figure 6e), measured in laboratory (e.g., Beeman et al., 1988; Durham et al., 1983) and used in a number of other numerical-based works (e.g., Bray et al., 2008), produces no match with the observed crater profile, and in particular no upper terrace developed. The modeled crater is smaller by up to ~25%, and both upper and lower crater walls exhibit a much higher slope, twice the value than the one expected from the topographic profile. In Figure 7, we summarize the trends of the depth-to-diameter ratio (Figure 7a), diameter (Figure 7b), and depth (Figure 7c), at varying Y_i of the non-porous ice (keeping constant all the other material parameters), where the values on the vertical axis are normalized to the corresponding value as measured on the observed impact structure. The solid line refers to the crater sizes, the dotted line to the pit dimensions. The panel 7a highlights that at the adopted value of 50 kPa, the crater depth-

to-diameter ratio (solid line) is minimized, while panel 7c shows that a variation of Y_i over the three orders of magnitude does not cause much variation in the crater depths.

Figure 8 shows how the damaged cohesion Y_d of each single layer affects the final crater morphology. In the first row, we vary the cohesion Y_d of the porous ice layer. A decrease in the cohesion Y_d from 10 kPa (Figure 8a) to 1 kPa (Figure 8c) causes a higher downward flow, which leads to a crater diameter increase of up to 10% with respect to the DTM profiles. In this case, no terrace nor morphological distinct feature between the two ice layers develop, notwithstanding the higher impendence contrast, while the upper crater wall inclination decreases by a factor of two. An increase of a factor of two in the damaged cohesion Y_d of the non-porous ice (Figures 8d and 8e) causes the non-porous ice layer to overturn and partially embed the porous ice layer. The interface between the two ice layers is marked only by a tiny kink, while the upper terrace forms at a shallower depth than what expected from the topographic elevation model of the crater, with a difference of ~80% in both cases. The crater diameter decreases by up to ~10% with respect to the DTM profile. For the above cases, the pit is ~10% larger than the measured crater profile, while its depth is ~1.5 times larger than the one measured on the DTM profile. Varying the damaged cohesion Y_d of the basaltic crust (Figures 8g and 8h) has as major outcome, significantly decreasing (~30%) the inclination of the lower crater wall, and decreasing the pit diameter by up to 20% with respect to the DTM profile. Figure 9 displays the trends of the depth-to-diameter ratio (Figure 9a), diameter (Figure 9b) and depth (Figure 9c) of crater (solid line) and pit (dotted line) dimensions at varying damaged cohesion (also in this case, normalized to the respective values derived from the DTM profiles). The color legend is taken similar to Figure 8, and is referred to by the three different target materials (pale blue: porous ice, blue: non-porous ice, and green: crust). Firstly, considering the trends when varying the damaged cohesion in the porous ice layer, we find that the depth-to-diameter ratio of the crater is minimized at a Y_d value lower than the one taken as best fit, although the one of the pit is minimized for the adopted value of 10 kPa. For the Y_d trend in the non-porous ice, we have only two data points, but we observe a decrease of the depth-to-diameter ratio with decreasing Y_d. Finally, the depth-to-diameter ratio of the crater remains constant within ~8% when the Y_d is varied in the basaltic crust, while the depth-to-diameter ratio of the central pit has a monotone growth.

Significant variations in the final crater morphology are also found by varying the damaged friction coefficient μ_d, consistent with previous expectations (e.g., Martellato et al., 2107). In Figure 10, we compare the variations of the μ_d within the range measured in the laboratory for ice and rock (see section 3.3) separately in each layer. The best fit model, shown in Figure 10a right panel, is obtained with a very low friction coefficient of both ice layers (0.18), and the implementation of a higher damaged friction coefficient for the basaltic crust (0.84). Indeed, by adopting the standard friction coefficient value of rocks (0.6, Figure 10a left panel), the central pit is ~78% larger and ~105% deeper than what expected from the topographic profile. While the depth increase obtained in this model is similar to what yielded the best fit, the diameter is much larger. A very large pit is also obtained in all the models with a 0.6 damaged friction coefficient of the basaltic crust (Figures 10c and 10d). While the damaged friction coefficient of the basaltic crust governs the size of the central pit, the damaged friction coefficient of both icy layers influenced the development of the upper and lower terraces. The upper terrace forms only when the damaged friction coefficient of the porous ice layer is low (0.18, Figure 10c left panel). The higher values of 0.35 and 0.6 of the damaged friction coefficient of the non-porous ice layer decreases the lower terrace width by ~50% and ~70%, respectively (Figures 10c and 10d), causing the crater to have an almost-bowl shaped morphology. In Figure 11, we report the depth-to-diameter ratio, diameter, and depth trends of the crater and the central pit. The crater depth-to-diameter ratio (pale blue solid line in Figure 11a) remains constant (with a maximum semi-dispersion of ~10%) when varying μ_d in the porous ice layer, although it has a minimum at the lowest tested value of 0.2. When considering the variations in the non-porous ice layer, the trends of the depth-to-diameter ratios of both crater and pit have a minimum at μ_d=0.35, although at this value no upper terrace develops. The crater diameter trend is slowly decreasing for increasing μ_d (blue solid line in Figure 11b), whereas the pit diameter trend is steepening with increasing μ_d (blue dotted line in Figure 11b).

583

584 **4.2 Crater 2**.

585 The stratigraphic sequence of the target modeled at the impact site of Crater 2 is similar to that of Crater 1 (cf.
586 Figure 3), made up of three layers of porous ice, non-porous ice, and basalt. The depth of the interface between
587 the stack of ice layers and the basaltic crust (indicated by the deeper floor terrace) in Crater 2 is ~40 m, the
588 same as that of Crater 1. However, the upper terrace in this crater is almost twice as deep (27 m versus 15 m).
589 Because we model the upper terrace as the interface between the porous and non-porous ice layers, this
590 therefore results in an increase of the thickness of the porous ice layer, and a corresponding decrease of the
591 thickness of the non-porous ice layer by about half in comparison to Crater 1 (13 m versus 25 m). In order to
592 assess the influence of a different depth of the horizon between porous and non-porous ice, we model Crater 2
593 with the same material model parameters used for Crater 1. At the same time, this choice is also supported by
594 the fact that the two craters formed in the same region (cf. Figure 1), and therefore the two impact sites might
595 likely have similar material properties.

596 Table S3 in the Supplemental material summarizes the numerical values of the features of Crater 2 for all the
597 models discussed in this section. The measurements of the crater features and their errors are computed as
598 described in Section 3.6 (cf. also Figure 3). In Figure 12 (and Figure 4d right panel), we report the last snapshot
599 (at t=25 s) for Crater 2 for the best fit model. The diameter of Crater 2 obtained with the best fit model is 5%
600 larger than the value measured in the terrain model. The upper terrace is wider by ~7%, and shallower by ~20%
601 with respect to the observed crater. The inclination of the upper wall is smaller by ~20%, while the one to the
602 lower wall is the same. Similar to Crater 1, the central pit generated by the model is much bigger than the
603 profile from the terrain model, with a diameter more than two times larger, and a depth as much as five times
604 deeper.

605 In Supplemental material, we report the detailed results about the dependence of the crater morphometry on the
606 intact cohesion Y_i, damaged cohesion Y_d, and friction coefficient μ_d, when varied independently in each target
607 layer. The trends of the morphometry variation for Crater 2 are similar to what obtained for Crater 1, with the
608 exception of the central pit, which develops much larger than in the first case study. Its diameter can be as
609 much as about four times that measured in the DTM profile, and its depth as much as about ten times.

610

611 **5. Discussion**

612 Small terraced craters in the Amazonian-aged Arcadia Planitia may indicate the presence of excess water ice,
613 on the basis of various observational evidence (e.g., Bramson et al., 2015, 2017; Dundas et al., 2015, 2018;
614 Feldman et al., 2011; Pathare et al., 2018; Viola et al., 2015). Here, we numerical modeled the formation of two
615 impact structures of very similar dimensions (~600−700 m in diameter), listed in the database compiled by
616 Bramson et al. (2015), in order to test the hypothesis that the transition between near-surface ice-rich layers and
617 the lower basaltic crust can generate terracing in Arcadia Planitia craters.

618 Before discussing the results, we would like to point out two assumptions. First, the two ice layers are
619 described by a different porosity and a different rheological model. The assumption of a 35% porous ice layer
620 atop a non-porous ice layer is based on the works of Bramson et al. (2015, 2017), who used a dielectric mixing
621 model to combine dielectric constants of air, dust, and ice in differing volumetric fractions, in order to match
622 the surface dielectric constants derived from SHARAD measurements. By this method, it is possible to only
623 place constraints on the overall composition of the entire strata above the subsurface radar interface.
624 Additionally, Bramson et al. (2017) extend these calculations, finding that the upper ice deposit needs a
625 porosity of 25−35% (and a dust content of 1−5%) to fit the low dielectric constants, and preserved the ice tens
626 of millions of years at mid-latitudes. A more recent study has thrown into question the ice concentrations in the

area (Campbell and Morgan, 2018), though Dundas et al. (2018) show that thick, pure ice deposits exist in the mid-latitudes. The assumption of two different ice rheologies relies on understanding the geological process that led to the target density profile just described. This might develop after the slow and gradual process of compaction at depths of snow into non-porous ice under increasing load caused by the continuous deposition of snow at the surface (e.g., Arthern et al., 2010). Here, we modeled an upper fully damaged porous ice layer atop a lower undamaged non-porous ice layer, though acknowledge that much remains to be discovered surrounding the properties and nature of mid-latitude ice on Mars.

Second, our results are obtained by assuming that the porous and non-porous ice layers are assumed to be water ice without any lithic component. However, this is a simplification. The ice is covered by a $\lesssim 1-2\,m$ thick dust layer (Bramson et al., 2017; Byrne et al., 2009; Dundas et al., 2014, 2018) that insulates and protects the ice, but this layer is not included in the simulations for model resolution reasons (a cell is 1.25 m and 0.94 m, respectively for Crater 1 and Crater 2). Additionally, the ice contains some amount of dust (though the concentration of dust and its variability, both laterally and vertically, is still an outstanding question). Although we will not consider this dust content in the next discussion, it is bearer of additional complexity to the whole story.

5.1 Crater morphology sensitivity to the Intact Cohesion of the Non-Porous ice

As observed in the crater formation process (Figure 4, and movie on the Supplemental material), variations in the near-surface target stratigraphy cause differences in the particle-velocity field and subsequent excavation flow. The craters develop a concentric terraced morphology, with an outer, larger crater in the low-cohesion region and an inner, smaller crater nested within the stronger basement material (forming essentially a central pit) from the early stages. A similar crater evolution was also observed by Senft & Stewart (2008), while Prieur et al. (2018) found that the concentric morphology evolved from the hemispherical transient cavity, during the modification stage. The best fit model, based on material parameters used in previous numerical studies, provides the better match in terms of crater morphology between the numerical and digital terrain models. The main difference lies in the value of the intact cohesion Y_i of the non-porous ice, which is lower than the strength measured in laboratory (5−25 MPa, e.g., Beeman et al., 1988; Jones, 1982; Durham et al., 1983), and the strength used in a number of other numerical investigations (10 MPa, e.g., Bray & Schenk, 2015; Bray et al., 2008, 2014), but it is similar to the Y_i adopted by Silber et al. (2017) to model crater formation in Europa (100 kPa). The low Y_i value of 50 kPa is adopted for the best fit model results to minimize the trend of the crater depth-to-diameter ratio, although the overall variation across the tested value is ~0.5 (Figure 7 and S2, solid line). The depth-to-diameter ratio of the central pit follows a similar trend, but shifted to higher value than what expected from the DTM profiles (Figure 7 and S2, dotted line). As shown in Figures 6 and S1, respectively for Crater 1 and Crater 2, the implementation of a higher intact cohesion Y_i causes a very poor fit with the DTM. For an intact cohesion of 10 MPa (Figures 6e and S1e), the modeled upper terrace in both cases is shallower by approximately 30% to 40%, and about 60% shorter in the case of Crater 1, with respect to the DTM profiles, while the upper and lower wall inclinations can be as steep as two times more. The failure in reproducing the upper terrace, and the inclination of the upper wall also causes a large mismatch in the crater diameter, with a difference of ~26% and ~8%, respectively for Crater 1 and Crater 2. In absolute values, this means a difference of ~180 m and ~50 m between the modeled and the measured crater diameters, respectively for Crater 1 and Crater 2. The generally-good results obtained by implementing a low intact cohesion Y_i in our models, together with the fact that the same value is used to explain complex crater collapse in Ganymede ("empirical method") by Bray et al. (2008), might indicate that the intermediate non-porous ice layer did not undergo a severe compaction.

5.2 Crater morphology sensitivity to the Damaged Cohesion

We test only a limited number of values of damaged cohesion Y_d for the non-porous ice layer, whereas seven orders of magnitude for the porous ice layer. For the best fit model, we use the same value of 10 kPa for both porous and non-porous ice layers. Although lower values for the damaged cohesion in the porous ice layer might have favored a more realistic depth-to-diameter ratio of the two craters (pale blue solid lines in Figures 9a and S4a), the central pit shape and dimensions do not gain any improvement by decreasing the damaged cohesion Y_d (pale blue dotted lines in Figures 9 and S4). The value of 10 kPa for Y_d, adopted also by Silber et al. (2017), is in between that of completely fragmented ice (0 MPa for the Martian surface, Senft & Stewart, 2008) and higher values (10 MPa in Ganymede, Bray et al., 2008), and it should account for the possible fracturing occurring in planetary contexts (Durham & Stern, 2001). As shown in Figures 8 and 9 for Crater 1, and Figures S3 and S4 for Crater 2, an independent increase in the damaged cohesion Y_d in the porous and non-porous ice layers causes a general decrease of the crater diameter (pale blue and blue solid lines in Figures 9b and S4b). In particular, we find that varying the damaged cohesion Y_d in the non-porous ice intermediate layer leads to the highest variation in the crater morphology, causing the upper terrace to develop at shallower depths than what observed in the actual crater. The difference might reach ~85%, which in absolute values means up to 20 m of difference between models and real crater, well above the model uncertainties. Prieur et al. (2018) found that the concentric morphology can develop when a damaged cohesion difference is greater than 0.05−0.45 MPa, or when normalized by the lithostatic pressure ($\Delta Y_{d0}/\rho g T$, with ΔY_{d0}= damaged cohesion difference, ρ=upper layer density, g=gravity acceleration, and T=upper layer thickness), greater than 0.03−0.27, when assuming and impact velocity of 12.7 km/s. In our models, if applying this formula, we derive a value of 0.03 for the interface between porous and non-porous ice, and 0.43 for the interface between non-porous ice and basalt, in agreement with the range proposed by Prieur et al. for the development of terraces at layer boundaries. According to these calculations, the double-terraced morphology might be expected in this target geometry. The outcome of the best fit model shows that doubling the thickness of the porous ice layer leads to a decrease of approximately a factor six in the upper terrace.

5.3 Crater morphology sensitivity to the damaged friction coefficient

With regards to the effects of the damaged friction coefficient μ_d on the crater morphology, for the porous and non-porous ice layers, we test the range of values derived in laboratory (0.2−0.55, Beeman et al., 1988; Durham & Stern, 2001). The value of 0.18 selected for the best fit model is slightly lower than the one measured in laboratory and used for modelling investigations (e.g., Luther et al. 2017). According to our analysis, the lower μ_d is firstly responsible for the development of the upper terrace at the correct depths observed in the DTM profiles (cf. Figures 10 and S5). At the same time, the effects of setting a value of 0.6 for the non-porous ice layers μ_d on the crater morphology can be also appraised from Figures 11 and S6: the crater depth-to-diameter ratio (blue solid lines, Figures 11a and S6a) remains constant within ~18% for both craters, but the pit diameter (blue dotted lines, Figures 11b and Sb) undergoes a severe enlargement (up to the 35%) with respect to the best fit. A similar trend is not observed when varying μ_d on the porous ice layer (pale blue lines, Figures 11 and S6). In this case, the pit diameter trends remain constant within 10%, but up to 1.5 times larger than the corresponding curves for the non-porous ice layer (dotted pale blue lines versus blue lines). This might be due to the fact that the variation of the depth-to-diameter and diameter with μ_d in the porous ice layer (pale blue lines) refers to a simulation suite with different material parameters than the ones used for the best fit model (cf. figures caption), where the μ_d for the basaltic crust is set to 0.6 as well. Indeed, as highlighted also in panels a, c and d of Figures 10 and S5, the damaged friction coefficient μ_d of the basaltic layer has a significant influence on the final pit dimensions: when adopting the standard value for rocks (0.6, e.g., Jaeger et al. 2007), the pit develops up to twice the diameter expected from the measured topographic profile, causing the lower terraced to have a negligible width.

718

719 **5.4 Central pit: morphology and key factors**

720 The friction coefficient is largely responsible for the dimensions of the central pit, and knowledge of the
721 damaged friction coefficient μ_d of each of the target layers is important for properly modeling the resulting
722 crater morphology. Changes to μ_d can cause the crater diameter to increase by a factor of five, and the depth by
723 a factor of ten, well above the uncertainties of models and DTM profiles. In the case of our best fit model for
724 Crater 1, the central pit is 208.9±2.5 m and 58.8±2.5 m, respectively, in diameter and depth, in comparison to
725 those observed in the terrain model of 198.9±12.3 m and 34.8±2.5 m. This means that the central pit is ~5%
726 larger and ~65% deeper, when compared to the respective topographic profile. In the case of Crater 2, the
727 discrepancy is much more severe, as it is possible to appreciate when comparing Figures 11 and 18, where the
728 diameter and depth trends of Crater 2 are much greater than those of Crater 1. The central pit derived from the
729 numerical simulations has a diameter of 122.7±1.9 m and a depth of 38.5±1.9 m, ~120% larger and ~430%
730 deeper than the central pit of the actual crater (being 56.2±9.5 m and 7.2±0.9 m, diameter and depth
731 respectively).

732 Such a significant discrepancy between the modeled and observed central pit morphology might be explained
733 by the poor knowledge of the target rheology and stratigraphy, and/or the projectile properties. The damaged
734 friction coefficient μ_d of the basaltic crust partly contributes to the final central pit shape and dimensions,
735 though it is not the only property influencing the pit morphometry. Indeed, we did not get a good fit in the case
736 of Crater 2. Additional complexities and/or variations in the target configurations, such as a different porosity
737 of the basaltic crust, the presence of embedded sheets of dust/regolith, or the activation of the dilatancy model,
738 do not lead to any improvement of the modeled central pit with the observed one (see Supplemental material
739 for the details on these simulations). Therefore, we consider whether the pit sizes might depend on the impact
740 geometry, or on the projectile material and density. In particular, whether the impactor properties might explain
741 the different degree of accuracy of the two modeled craters with the respective DTM profile. In iSALE-2D, due
742 to its 2D nature, oblique impacts can be simulated by varying the vertical speed. We test the formation of
743 Crater 2, adopting the lower impact velocity of 5 km/s (corresponding to the vertical component of a 30°
744 impact), finding a decrease of 25% of the central pit dimensions (see Supplemental material for more details).
745 Therefore, a larger and slower (and/or more oblique) projectile might partly account for getting a better fit for
746 the central pit.

747 The impactor properties, like material and density, might have an important role to the development of this
748 feature too. Indeed, after Melosh (1989), the penetration depth d_p of the impactor depends on its diameter L
749 through the formula: $d_p = L\sqrt{\varrho_p/\varrho_t}$, where ϱ_p and ϱ_t are the densities of the projectile and the target,
750 respectively (cf., equation 7.3.1 at pag. 114 in Melosh 1989). According to this equation, a large portion of the
751 initial kinetic energy is deposited on the basaltic layer in our current model setup. However, a different impact
752 scenario with a smaller, lower-density and faster projectile would lead to a lower penetration depth. To test this
753 hypothesis, we implemented a simulation using a comet-like impactor. The impact velocity is set to 28 km/s
754 (Steel, 1998), which requires a projectile radius of 6 m to fit the crater diameter. Figure 13 shows the
755 comparison of the craters obtained using either basalt (left panel, corresponding to the model used so far in the
756 paper) or non-porous ice (right panel) composition for the projectile, as a proxy for asteroids and comets,
757 respectively. Overall, the two projectile materials yield very similar results in terms of crater diameter and rim
758 height, upper terrace width, and inclinations of both upper and lower crater wall inclination. In this case, the
759 central pit does not develop at all in the case of an icy projectile, providing support to the fact that a different
760 suite of projectile parameters can have a leading role in controlling the pit dimensions.

761

762 **5.5 Crater rim**

The modeled crater rims are higher than the one observed in the topographic profiles, with a difference of 0.4−2.1 times the rim of Crater 1, and 1.9−7.8 times the rim of Crater 2. For the specific best fit model, the crater rim is 1.2 and 4.4 times higher than the one measured in the DMT profile, respectively for the two cases. In absolute values, this means a difference of 1.3 m and 4.8 m, for Crater 1 and Crater 2, respectively.

As noticed in Figure 4, and in the crater formation video on the Supplemental material, the crater rim and proximal ejecta of both craters are mainly composed of the ice, with randomly spaced rocky chunks originated as high velocity ejecta from the basaltic crust. Therefore, the difference between the rims of the modeled craters and their respective DTMs may be partly ascribed to ice sublimation processes.

However, the rims of the two craters are reproduced with a different accuracy. This might be due to different ages of the two impact structures (and therefore a different degree of degradation), and/or the presence of a thicker surficial dust/regolith at the site of Crater 1. Both studied craters exhibit a thin ejecta deposit that might extend up to about five times the crater radius beyond the crater rim (Figure 2), exhibiting a dune-like morphology in the proximal ejecta, while a subradial facies beyond in the distal deposits, starting at about two crater radii from the crater center. This behavior implies the presence of a high lithic content in the near-surface area that behaves as a protective sheet preventing or slowing down ice sublimation (e.g., Kadish et al., 2010; Nunes et al., 2011). As for instance, Chevrier et al. (2007) found that regolith layers inhibit ice loss rate up to a factor of 8, and that at temperature between 160−170 K, the humidity precludes ice sublimation. Barlow et al. (2014) investigated layered ejecta smoothing into a thin deposit, which ends with a sinuous appearance too. This special pattern, called by the author as “Low-Aspect-Ratio Layered Ejecta” (LARLE), was suggested to develop after an impact into ice- and dust-rich mantling deposits, and can then turn into the pedestal ejecta morphology during lower obliquity periods when ice sublimates (Boyce et al., 2015). However, Crater 1 shows a very well-preserved and defined ejecta deposit, with a characteristic rough and hummocky morphology, which is not as clearly distinguishable around Crater 2. From observations, the basaltic crust is at the same depth for both impact structures. Hence, given Crater 1 is larger than Crater 2 (~710 m versus ~590 m), it would excavate material from a depth ~1.2 times deeper (57.0 m versus 47.1 m, if assuming an excavation depth $H_{exc} \sim {}^{1}/_{10}\, D_t$, and a transient diameter $D_t \sim 0.8D$, e.g., Melosh, 1989). Additionally, on the south-eastern zone of the ejecta deposit surrounding Crater 1, another small single-terraced crater (~350 m in diameter and ~14 m in depth, cf. Figure 2c) is present, whose morphology suggests the presence of an upper layer (perhaps the protective dust/regolith surface covering) with distinct properties, including fracturing degree, density and composition, from the underlying layer.

5.6 Martian Climate Evolution

Although the two craters are only ~140 km away, the subsurface structure (thicknesses of the porous and non-porous ice layers) is different, with the top weaker layer ~10 m thinner at the site of Crater 1 compared to Crater 2. This suggests the two sites have experienced different amounts or timing of ice accumulation, or ice modification (e.g. compaction, fracturing, etc.), due to local variability in surface and atmospheric processes. The value of 8−12 mm/yr for ice accumulation in the Arcadia Planitia region in a moderate obliquity (25°−35°) found by the Global Circulation Models of Madeleine et al. (2009) would translate into a minimum of a ~1 kyr longer period of ice/snow accumulation at Crater 2 area to account for the 10 m thicker stratum of the porous ice at that site (with a longer timeframe needed depending on the amount of densification experienced by this layer compared to the density at which it is deposited).

We can alternatively, or additionally, consider that at the Crater 1 location a larger amount of lithic component was incorporated into the ice, which would therefore grow a thicker dust covering during periods of instability, better preserving the ice from further sublimation. A lower amount of lithic content at the Crater 2 location might be also supported by the fact that Crater 2 rim is completely flattened at the level of the surface (e.g.,

DTM profile in Figure 12). Additionally, many additional processes might affect the local rates of ice deposition, sublimation, and evolution, including the presence of salts to generate pre-melt films around the ice grains and/or aid in sintering and/or differences in the mass balance of the ice. The entire ice layer is likely the result of a complicated and continuous process of multiple periods of deposition, removal, and modification during different obliquity periods among the late Amazonian era (e.g., Head et al., 2003; Kadish et al., 2010). Future modeling that accounts for vertically-heterogeneous ice-dust mixtures could yield useful insights to the role that lithic material embedded in ice-rich target materials plays on the crater formation process.

6. Conclusion

Relatively small, simple craters develop concentric, or terraced, morphologies due to the different response of shock waves encountering target layers of different composition, density and/or rheology, with the deeper substratum having higher strength (e.g., Lange & Ahrens, 1987; Oberbeck & Quaide, 1967; Senft & Stewart, 2008).

In this study, we select two double-terraced craters (Crater 1: D_c=713 m, Crater 2: D_c=588 m) from the Bramson et al. (2005) database for Arcadia Planitia, a northern mid-latitude region of Mars with numerous lines of evidence for shallow subsurface ice. The lower terrace occurs at the same depth of ~40 m for both craters, and is hypothesized to be the interface between material properties also responsible for the subsurface radar reflectors measured by the Shallow Radar (SHARAD) instrument (Bramson et al., 2015). The low bulk dielectric constant derived from SHARAD measurements, together with surficial geomorphological structures in the region, led that study to the conclusion that the deeper terrace may be the interface between a relatively clean ice (with a dust content of 1−5% in the total volume of ice) layer overtop the stronger, basaltic bedrock (Bramson et al. 2015). The smaller, upper crater terrace, which is located at different depths for the two craters, might represent a transition in the ice properties: from a younger surficial porous (~35%) ice layer over denser (non-porous) ice (Bramson et al., 2015).

We numerically model the formation of these two impact craters by means of the iSALE shock physics code (Amsden et al., 1980; Collins et al., 2004, 2011; Wünnemann et al., 2006). For an assumed vertical impact speed of 7 km/s and impactor density of ~2500 kg/m^3, our best-fit models are for a projectile radius of 20 m and 15 m, respectively for Crater 1 and Crater 2. Our simulations reproduce the morphology of the crater walls and terracing very well. We find that the inclination of the upper wall is mainly controlled by the intact and damaged cohesions of the non-porous ice layer, while the depth and size of the upper terrace is mainly controlled by the damaged friction coefficient of both the porous and non-porous ice layers. However, the modeled central pit is up to two times larger than the observed ones. Although the target properties, like the damaged friction coefficient of the bedrock and local stratigraphic variations, may be partly responsible for the poor fit, we find that the projectile properties, including density, material and impact speed, play a key role in the formation and final size of the central pit.

Our modeling lends support to the presence of excess water ice in the near surface in Arcadia Planitia as a plausible explanation for the terraced crater morphologies which are abundant across the region. The different stratigraphies at the two impact sites might suggest a temporal and spatial variability of ice deposition and evolution. In particular, the possible presence of a higher lithic content at Crater 1 region, as suggested also by the morphology of its ejecta blanket, could have caused a different sublimation rate between the two impact sites, and influenced the process of ice deposition/removal during different high obliquity periods among the late Amazonian era. Future modeling that accounts for vertically-heterogeneous ice-dust mixtures could yield useful insights to the role that lithic material embedded in ice-rich target materials plays on the crater formation process.

Acknowledgments

We gratefully acknowledge the developers of iSALE-2D/Chicxulub version (www.isale-code.de), including Gareth Collins, Kai Wünnemann, Dirk Elbeshausen, Boris Ivanov, and Jay Melosh. Some plots in this work were created with the pySALEPlot tool written by Tom Davison.

The manuscript was significantly improved by the comments from the Associated Editor Gareth Collins, Nadine Barlow and an anonymous Reviewer. We gratefully acknowledge the Editor David Baratoux. The authors would like to acknowledge Sarah Sutton and the HiRISE Operation Center Digital Terrain Model (DTM) lab for help in the creation and validation of the DTMs which informed this study. E.M. acknowledges Tomke Lompa for computer and logistic support.

E.M. acknowledges the University of Padova under the 2013 Junior Fellowship, and INAF-Osservatorio Astronomico di Padova under grants I/022/10/2 BepiColombo, and 2013-056-RO JUICE. E. M. has also partly received funding from the European Union's Horizon 2020 research and innovation Programme under the Marie Skłodowska-Curie grant agreement No 709122 to complete this work. A.M.B. would like to acknowledge the American NSF Graduate Research Fellowship under grant DGE-1143953, and a NASA Earth and Space Sciences Fellowship (NESSF) under grant NNX16AP09H.

Figure Caption

Figure 1. Map of terraced craters, with diameter ranging from few hundreds of meters up to less than 1 km, in Arcadia Planitia (modified from Bramson et al., 2015). The different symbols refer to a different crater classification: questionable, single-terraced craters, double-terraced craters. The red and the blue stars indicate the location of Crater 1 and Crater 2, respectively, which are the two double-terraced impact structures modeled in this study.

Figure 2. HiRISE images of the two double-terraced simple craters in Arcadia Planitia modelled in this study: (a) image ESP_018522_2270, (b) image ESP_033805_2285, (c) zoom on crater 1; (d) zoom on crater 2. *Image credit*: NASA/JPL/University of Arizona.

Figure 3. Sketch of the morphology of a double-terraced crater in Arcadia Planitia, where the specific terms used in the text for each element of the craters are indicated, along with values of the diameters and depths of the two studied craters (cf. the first line in Table S2 and S3 in the Online Material). Here in the following, the definition of the symbols: D_c and R_c are the crater rim-to-rim diameter and rim height, respectively; R_0 represents the crater radius at the pre-impact surface; d_{UT}, d_{LT}, and d_c are the depth of the upper terrace, the lower terrace, and the crater floor, respectively, and all these depths are measured from the pre-impact surface;

Δ_{UT} and Δ_{LT} are the width of the upper and the lower terraces, respectively; α_U and α_L are the inclination of the upper and the lower walls, respectively; D_{pit}, R_{pit} and d_{pit} are the diameter, rim and depth of the central pit, respectively (R_{pit} and d_{pit} are both measured from the elevation of the lower terraced). The sketch of the double-terraced crater is not to scale.

Figure 4. Snapshots of the crater-forming process for Crater 1 (left panel of each plots) and Crater 2 (right panel of each plots), at different time steps, from the contact stage (t=0 s, panel a), to cavity expansion through material displacement (t=0.5 s, panel b) and ejecta deposition (t=9 s, panel c), and to collapse of the material up to the final end (t=25 s, panel d). The final morphology of the two modeled craters showed the development of two terraces at the two boundary interfaces between porous and non-porous ice, and between ice and crust, and is compared to the digital terrain model (DTM) profiles (red lines in panel d). The error in the DTM was given by the maximum semi-dispersion. For both DTM profiles and modeled craters, the diameter is measured rim-to-rim, while the depth is given by the distance of the crater floor from the pre-impact surface. The simulation showed in this figure is referred to the best fit model: the projectile radius is 20 and 15 m, respectively for Crater 1 and Crater 2. Model parameters (cf. Table 1 and section 3.3 for symbol description): *crust*: Y_{0i}=20 MPa, μ_i=1.4, Y_{0d}=0.2 MPa, μ_d=0.84; *non-porous ice*: Y_{0i}=50 kPa, μ_i=2.0, Y_{0d}=10 kPa, μ_d=0.18; *porous ice*: Y_{0d}=10 kPa, μ_d=0.18. The plot colors are referred to the three different materials: cyan for the porous ice, blue for the non-porous ice, and green for the basaltic crust.

Figure 5. Final snapshot of the best fit model for Crater 1 (see caption of Figure 5 and Table 1 for the model values), overlaid by the DTM profile (red line). The left panel shows the three different target material: porous ice (cyan), non-porous ice (blue), and basaltic crust (green). The right panel shows damage accumulation, in a color scale given by the legend. The morphometric measures are given in the second row of Table S2 in the Online Material.

Figure 6. The picture shows the final step (t=25 s) of Crater 1 for a number of models where the intact strength Y_i of the basaltic crust (with superscript "*cr*"), and the non-porous ice ("*npi*") layers was tested. The model parameters of reference are the ones of the best fit model, given in Table 1, and showed here in plot (a). The model results by varying the Y_i are shown in plots (b) to (e), and the specific values are provided in each plot. The plot colors are referred to the three different materials: cyan for the porous ice, blue for the non-porous ice, and green for the basaltic crust. The red line is the DTM profile.

Figure 7. The picture displays the curves for Crater 1 of the (a) depth-to-diameter ratio, (b) diameter, and (c) depth, as a function of the intact cohesion Y_i of the non-porous ice, while all the other parameters are kept constant to the best fit values (cf. caption of Figure 5). The blue solid line refers to the crater dimensions, while the blue dotted line to the central pit dimensions. The values of each plot are normalized to the respective values derived from the DTM profile (D_c=710.4 m, d_c=82.1, d_c/D_c=0.12, D_{pit}=203.3, d_{pit}=33.2, d_{pit}/D_{pit}=0.16). The three vertical axes have not the same scale.

Figure 8. The picture shows the final step (t=25 s) of Crater 1 for a number of models where the cohesion Y_d of the three different layers was tested: (i) porous ice (with superscript "*pi*"), (ii) non-porous ice ("*npi*"), and (iii) basaltic crust ("*cr*"). The model parameters of reference are the ones of the best fit model, given in Table 1, while the varied values are provided in each panel. Models in the panels a, f, and i are the best fit model. The

plot colors are referred to the three different materials: cyan for the porous ice, blue for the non-porous ice, and green for the basaltic crust. The red line is the DTM profile.

Figure 9. The picture displays the curves for Crater 1 of the (a) depth-to-diameter ratio, (b) diameter, and (c) depth. The horizontal axis represents the damaged cohesion Y_d on a logarithmic scale. Values on the vertical axis are normalized to the respective values derived from the DTM profile (D_c=710.4 m, d_c=82.1, d_c/D_c=0.12, D_{pit}=203.3, d_{pit}=33.2, d_{pit}/D_{pit}=0.16). The three vertical axes have not the same scale. Legend for the line style: solid lines refer to crater dimensions, dotted lines refer to central pit dimensions. Legend for the line color: pale blue indicates the porous ice layer, blue the non-porous ice layer, and green the basaltic crust (consistent with the general color choice used throughout all the paper).

Figure 10. The picture shows the final step (t=25 s) of Crater 1 for a number of models where the damaged friction coefficient μ_d of the three different layers was tested: (i) porous ice (with superscript "*pi*"), (ii) non-porous ice ("*npi*"), and (iii) basaltic crust ("*cr*"). For each plot (a) to (d), the μ_d values in two of the three layers were kept constant (given as title of each plot), and the μ_d values of the third layer was varied (provided in each plot). The model parameters of reference are the ones of the best fit model, given in Table 1. The right panel in plot (a) represents the best fit model. The plot colors are referred to the three different materials: cyan for the porous ice, blue for the non-porous ice, and green for the basaltic crust. The red line is the DTM profile.

Figure 11. The picture displays the trends of the (a) depth-to-diameter ratio, (b) diameter, and (c) depth of the porous ice layers (pale blue lines) and the non-porous ice layer (blue lines) of Crater 1. The trends are shown for varying damaged friction coefficient μ_d, keeping constant all the other material model parameters. In the case of the non-porous ice simulations, data refers to the best fit model. In the case of the porous ice, simulations are run with different material model parameters: *crust*: Y_{0i}=10 MPa, μ_i=1.2, Y_{0d}=5 MPa, μ_d=0.6; *non-porous ice*: Y_{0i}=50 kPa, μ_i=2.0, Y_{0d}=50 kPa, μ_d=0.6; *porous ice*: Y_{0d}=0 kPa, μ_d=0.2÷0.6. This suite of simulations was run with a 10 CPPR projectile, and is included here because it has a higher number of data point for μ_d variation, and also to show the difference with the best fit model. The vertical values are normalized to the respective values derived from the DMT profile (D_c=710.4 m, d_c=82.1, d_c/D_c=0.12, D_{pit}=203.3, d_{pit}=33.2, d_{pit}/D_{pit}=0.16). The three vertical axes have not the same scale. Solid lines refer to crater dimensions, dotted lines to the central pit dimensions.

Figure 12. Final snapshot of the best fit model for Crater 2 (see caption of Figure 5 and Table 1 for the model values), overlaid by the DTM profile (red line). The left panel shows the three different target material: porous ice (cyan), non-porous ice (blue), and basaltic crust (green). The right panel shows damage accumulation, in a color scale given by the legend. The morphometric measures are given in the second row of Table S3 in the Online Material.

Figure 13. Final snapshot of the best fit model for Crater 2 (see caption of Figure 5 and Table 1 for the model values), overlaid by the DTM profile (red line). The left panel shows the best fit model in standard conditions, i.e. using an asteroidal projectile (here modeled with a basaltic composition), while the right panel shows the same model, but adopting a cometary projectile (which was modeled as non-porous ice). In this second case, the impact velocity was set to 28 km/s, corresponding to the 45° component of the average velocity of near-parabolic comets on Mars (Steel, 1998). The plot colors are referred to the three different materials: cyan for

the porous ice, blue for the non-porous ice, and green for the basaltic crust. Note: the ice-projectile simulation showed on the right panel is at a 10 CPPR, and the time of the snapshot is 20 s. The crater has not yet finished to form, but, due to computational issues, it was not possible to continue anymore this run. However, this does not preclude the discussion and outcome presented in the text, since the central pit has not developed.

References.

Amsden, A. A., Ruppel, H. M., & Hirt, C. W. (1980). SALE: A simplified ALE computer program for fluid flow at all speeds. Los Alamos National Laboratory Report, LA-8095 (101 pp.).

Andrews-Hanna, J. C., Zuber, M. T., Arvidson, R. E., & Wiseman, S. M. (2010). Early Mars Hydrology: Meridiani playa deposits and the sedimentary record of Arabia Terra. *Journal of Geophysiscal Research, 115*(E6), E06002, 1-22. https://doi.org/10.1029/2009JE003485

Arakawa, M., & Maeno, N. (1997), Mechanical strength of polycrystalline ice under uniaxial compression. *Cold Regions Science Technology, 26(3),* 215-229. https://doi.org/10.1016/S0165-232X(97)00018-9

Arakawa, M., & Tomizuka, D. (2004). Ice-silicate fractionation among icy bodies due to the difference of impact strength between ice and ice-silicate mixture. *Icarus, 170(1),* 193-201. https://doi.org/10.1016/j.icarus.2004.02.009

Artemieva, N., Karp, T., & Milkereit, B. (2004). Investigating the lake Bosumtwi impact structure: Insight from numerical modeling. *Geochemistry, Geophysics, Geosystems, 5*, Q11016. https://doi.org/10.1029/2004GC000733

Arthern R. J., Vaughan, D. G., Rankin, A. M., & Mulvaney, R. (2010). In situ measurements of Antarctic snow compaction compared with predictions of models. *Journal of Geophysical Research: Earth Surface, 115*(F3), F03011. https://doi.org/10.1029/2009JF001306

Baratoux, D., Samuel, H., Michaut, C., Toplis, M. J., Monnereau, M., Wieczorek, M., Garcia, R., & Kurita, K. (2014). Petrological constraints on the density of the Martian crust. *Journal of Geophysical Research: Planets, 119*, 1707-1727. https://doi.org/10.1002/2014JE004642

Barker, D. C., & Bhattacharya, J. P. (2018). Sequence stratigraphy on an early wet Mars. *Planetary and Space Science, 151*, 97-108. https://doi.org/10.1016/j.pss.2017.11.012

Barlow, N. G., Boyce, J. M., & Cornwall, C. (2014). Martian Low-Aspect-Ratio Layered Ejecta (LARLE) craters: Distribution, characteristics, and relationship to pedestal craters. *Icarus*, 239, 186-200. https://doi.org/10.1016/j.icarus.2014.05.037

Barlow, N. G., Ferguson, S. N., Horstman, R. M., & Maine, A. (2017). Comparison of central pit craters on Mars, Mercury, Ganymede, and the Saturnian satellites. *Meteoritics & Planetary Science, 52(*7), 1371-1387. https://doi.org/10.1111/maps.12857

Bart, G. D., Nickerson, R. D., Lawder, M. T., & Melosh, H. J. (2011). Global survey of lunar regolith depths from LROC images. *Icarus, 5(2),* 485-490. https://doi.org/10.1016/j.icarus.2011.07.017

Beeman, M., Durham, W. B. & Kirby, S. H. (1988). Friction of ice. *Journal of Geophysiscal Research, 93*, 7625–7633. https://doi.org/10.1029/JB093iB07p07625

Binzel, R. P., A'Hearn, M., Asphaug, E., Barucci, M. A., Belton, M., Benz, W., Cellino, A., Festou, M. C., Fulchignoni, M., Harris, A. W., Rossi, A., & Zuber, M. T. (2003). Interiors of small bodies: foundations and perspectives. *Planetary and Space Science, 51*, 443-454. https://doi.org/10.1016/S0032-0633(03)00051-5

Bland, P. A., & Smith, T. B. (2000). Meteorite Accumulations on Mars. *Icarus, 144*(1), 21-26. https://doi.org/10.1006/icar.1999.6253

Bottke, W. F., Nolan, M. C., Greenberg, R., & Kolvoord, R. A. (1994). Velocity distributions among colliding asteroids. *Icarus, 107*(2), 255-268. https://doi.org/10.1006/icar.1994.1021

Boyce, J. M., Wilson, L., & Barlow, N. G. (2015). Origin of the outer layer of Martian Low-Aspect Ratio Layered Ejecta craters. *Icarus, 245*, 263-272. https://doi.org/10.1016/j.icarus.2014.07.032

Bramson, A. M., Byrne, S., Putzig, N. E., Sutton, S., Plaut, J. J., Brothers, T. C., & Holt, J. W. (2015), Widespread excess ice in Arcadia Planitia, Mars. *Geophysical Research Letters, 42*(16), 6566-6574. https://doi.org/10.1002/2015GL064844

Bramson, A. M., Byrne, S., & Bapst, J. (2017). Preservation of Midlatitude Ice Sheets on Mars. *Journal of Geophysical Research: Planets, 122*(11), 2250-2266. https://doi.org/10.1002/2017JE005357

Bray, V. J., Collins, G. S., Morgan, J. V., & Schenk, P. M. (2008). The effect of target properties on crater morphology: Comparison of central peak craters on the Moon and Ganymede. *Meteoritics & Planetary Science, 43*(12), 1979-1992. https://doi.org/10.1111/j.1945-5100.2008.tb00656.x

Bray, V .J., Collins, G. S., Morgan, J. V., Melosh, H. J., & Schenk, P. M. (2014). Hydrocode simulation of Ganymede and Europa cratering trends – How thick is Europa's crust?, *Icarus 231*, 394-406. https://doi.org/10.1016/j.icarus.2013.12.009

Bray, V. J., & Schenk, P. M. (2015). Pristine impact crater morphology on Pluto—Expectations for new horizons, *Icarus, 246*, 156-164. https://doi.org/10.1016/j.icarus.2014.05.005

Britt, D.T., Yeomans, D., Housen, K., & Consolomagno, G. (2002). *Asteroid Density, Porosity, and Structure*. In W. F. Bottke Jr., A. Cellino, P. Paolicchi & R. P. Binzel (Eds.), *Asteroids III* (pp. 485-500), University of Arizona Press, Tucson.

Byrne, S., Dundas, C. M., Kennedy, M. R., Mellon, M. T., McEwen, A. S., Cull, S. C., et al. (2009). Distribution of Mid-Latitude Ground Ice on Mars from New Impact Craters. *Science, 325*(5948), 1674-1676. https://doi.org/10.1126/science.1175307

Campbell, B. A., & Morgan, G. A. (2018). Fine-scale layering of Mars polar deposits and signatures of ice content in nonpolar material from multiband SHARAD data processing. *Geophysical Research Letters, 45*. 1759-1766. https://doi.org/10.1002/2017GL075844

Chandnani, M., Herrick, R. R. M., & Kramer, G. Y. (2019). Geologic Analyses of the Causes of Morphological Variations in Lunar Craters Within the Simple-to-Complex Transition. *Journal of Geophysical Research: Planets, 124(E5)*, 1238-1265. https://doi.org/10.1029/2018JE005729

Chevrier, V., Ostrowski, D. R., & Sears, D. W. G. (2007). Experimental study of the sublimation of ice through an unconsolidated clay layer: Implications for the stability of ice on Mars and the possible diurnal variations in atmospheric water. *Icarus, 196*, 459-476. https://doi.org/10.1016/j.icarus.2008.03.009

Clifford, S. M. (1993). A model for the hydrologic and climatic behavior of water on Mars. *Journal of Geophysiscal Research, 98*(E6), 10973-11016. https://doi.org/10.1029/93JE00225

Collins, G. S. (2014). Numerical simulations of impact crater formation with dilatancy. *Journal of Geophysiscal Research: Planet, 119*, 2600-2619. https://doi.org/10.1002/2014JE004708

Collins, G. S., Melosh, H. J., & Ivanov, B. A. (2004). Modeling damage and deformation in impact simulations. *Meteoritics & Planetary Science, 39*(2), 217-231. https://doi.org/10.1111/j.1945-5100.2004.tb00337.x

Collins, G. S., Kenkmann, T., Osinski, G. R., & Wünnemann, K. (2008). Mid–sized complex crater formation in mixed crystalline–sedimentary targets: Insight from modeling and observation. *Meteoritics & Planetary Science, 43*(12), 1955-1977. https://doi.org/10.1111/j.1945-5100.2008.tb00655.

Collins, G. S., Melosh, H. J., & Wünnemann, K. (2011). Improvements to the ε-α porous compaction model for simulating impacts into high-porosity solar system objects. *International Journal of Impact Engineering, 38*(6), 434-439. https://doi.org/10.1016/j.ijimpeng.2010.10.013

Collins, G. S., Elbeshausen, D., Davison, T. M., Wünnemann, K., Ivanov, B. A., & Melosh H.J. (2016). iSALE-Dellen manual. *Figshare*. https://doi.org/10.6084/m9.figshare.3473690

Consolomagno, G. J., Britt, D. T., & Macke, R. J. (2008). The significance of meteorite density and porosity. *Geochemistry, 68*(1), 1-29. https://doi.org/10.1016/j.chemer.2008.01.003

Coulson, I. M., Beech, M., & Nie, W. (2007). Physical properties of Martian meteorites: Porosity and density measurements. *Meteoritics & Planetary Science, 42*(12), 2043-2054. https://doi.org/10.1111/j.1945-5100.2007.tb01006.x

Cremonese, G., Martellato, E., Marzari, F, Kuhrt, E., Scholten, F., Preusker, F., Wünnemann, K., Borin, P., Massironi, M., Simioni, E., Ip, W., & the OSIRIS team (2012). Hydrocode simulations of the largest crater on asteroid Lutetia. *Planetary and Space Science, 66(1)*, 147-154. https://doi.org/10.1016/j.pss.2012.01.001

Croft, S. K., Kieffer, S. W., & Ahrens, T. J. (1979). Low-velocity impact craters in ice and ice-saturated sand with implications for martian crater count ages. *Journal of Geophysical Research, 84*, 8023–8032. https://doi.org/10.1029/JB084iB14p08023

Davis, P. M. (1993). Meteoroid impacts as seismic sources on Mars. *Icarus, 105*(2), 469-478. https://doi.org/10.1006/icar.1993.1142

Davison, T. M., Collins, G. S., & Ciesla, F. J. (2010). Numerical modelling of heating in porous plantesimal collisions. *Icarus, 208*, 468-481. https://doi.org/10.1016/j.icarus.2010.01.034

Davison, T. M., Ciesla, F. J., & Collins, G. S. (2012). Post-impact thermal evolution of porous planetesimals, *Geochim Cosmochim Acta, 95*, 252-269, doi: 10.1016/j.gca.2012.08.001

Dundas, C. M., Byrne, S., McEwen, A. S., Mellon, M. T., Kennedy, M. R., Daubar, I. J., & Saper, L. (2014). HiRISE observations of new impact craters exposing Martian ground ice. *Journal of Geophysical Research: Planets, 119*(1), 109-127. https://doi.org/10.1002/2013JE004482

Dundas, C. M., Byrne, S., & McEwen, A. S. (2015). Modeling the development of martian sublimation thermokarst landforms. *Icarus 262*, 154-169. https://doi.org/10.1016/j.icarus.2015.07.033

Dundas, C. M., Bramson, A. M., Ojha, L., Wray, J. J., Mellon, M. T., Byrne, S., et al. (2018). Exposed subsurface ice sheets in the Martian mid-latitudes. *Science, 359*(6372), 199-201. https://doi.org/10.1126/science.aao1619

Drucker, D. C., & Prager, W. (1952). Soil mechanics and plastic analysis or limit design. *Quarterly of Applied Mathematics, 10*, 157-165. https://www.jstor.org/stable/43633942

Durham, W. B., Heard, H. C., & Kirby, S. H. (1983). Experimental deformation of polycrystalline H_2O ice at high pressure and low temperature: Preliminary results. *Journal of Geophysical Research, 88*, B377-B392. https://doi.org/10.1029/JB088iS01p0B377

1099 Durham, W. B., & Stern, L. A. (2001). Rheological Properties of Water Ice—Applications to Satellites of the
1100 Outer Planets, *Annual Review of Earth and Planetary Sciences, 29,* 295-330.
1101 https://doi.org/10.1146/annurev.earth.29.1.295

1102 Fassett, C., Needham, D. H., Watters, W. A., & Hundal, C. (2017). Exploring Regolith Depth and Cycling on
1103 Mars, *Am Geophys Union, Fall Meeting 2017*, abstract #P41E-2866

1104 Feldman, W. C., Pathare, A., Maurice, S., Prettyman, T. H., Lawrence, D. J., Milliken, R. E., & Travis, B. J.
1105 (2011). Mars Odyssey neutron data: 2. Search for buried excess water ice deposits at nonpolar latitutes on
1106 Mars. *Journal of Geophysical Research, 116*(E11), E11009, 1-17. https://doi.org/10.1029/2011JE003806

1107 Flynn, G. J., & McKay, D. S. (1990). An assessment of the meteoritic contribution to the Martian soil. *Journal*
1108 *of Geophysical Research, 95*, 14497-14509. https://doi.org/10.1029/JB095iB09p14497

1109 Goossens, S., T. J. Sabaka, A. Genova, E. Mazarico, J. B. Nicholas, & G. A. Neumann (2017). Evidence for a
1110 low bulk crustal density for Mars from gravity and topography. *Geophysical Research Letters, 44*, 7686–7694.,
1111 https://doi.org/10.1002/2017GL074172

1112 Greeley, R. (2013). *Introduction to planetary geomorphology*. Cambridge, UK. Cambridge University Press.
1113 238 pp.

1114 Greeley, R., & Spudis, P. D. (1981). Volcanism on Mars. *Reviews of Geophysics and Space Physics, 19*, 13-41.
1115 https://doi.org/10.1029/RG019i001p00013

1116 Grey, I. D. S., & Burchell, M. J. (2003). Hypervelocity impact cratering on water ice targets at temperatures
1117 ranging from 100 K to 253 K. *Journal of Geophysical Ressearch: Planet, 108(E3),* 5019.
1118 https://doi.org/10.1029/2002JE001899.

1119 Grotzinger, J. P., Arvidson, R. E., Bell, J. F., Calvin, W., Clark, B. C., Fike, D. A., et al. (2005). Stratigraphy
1120 and sedimentology of a dry to wet eolian depositional system, Burns formation, Meridiani Planum, Mars. *Earth*
1121 *and Planetary Science Letters, 240*(1), 11-72. https://doi.org/10.1016/j.epsl.2005.09.039

1122 Haehnel, R. B., & Shoop, S. A. (2004). A macroscale model for low density snow subjected to rapid loading.
1123 *Cold Regions Science and Technology, 40*, 193-211. https://doi.org/10.1016/j.coldregions.2004.08.001

1124 Hartmann, W. K. (1973). Ancient Lunar Mega-Regolith and Subsurface Structure. *Icarus, 18*(4), 634-636.
1125 https://doi.org/10.1016/0019-1035(73)90066-3

1126 Head, J. N., Melosh, H. J., & Ivanov, B. A. (2002). Martian Meteorite Lauch: High-Speed Ejecta from Small
1127 Craters. *Science, 298*, 1752-1756. https://doi.org/10.1126/science.1077483

1128 Head, J. W., Mustard, J. F., Kreslavsky, M. A., Milliken, R. E., & Marchant, D. R. (2003). Recent ice ages on
1129 Mars. *Nature, 426*(6968), 797-802. https://doi.org/10.1038/nature02114

1130 Herrick, R. R., & Hynek, B. M. (2017). Investigating target versus impactor influences on Martian crater
1131 morphology at the simple-complex transition, *Meteoritics & Planetary Science, 52*(8), 1722-1743.
1132 https://doi.org/10.1111/maps.12884

1133 Hiesinger, H., Head, J. W., & Wolf, U. (2001). Lunar mare basalts: Mineralogical variations with time, *32nd*
1134 *Lunar and Planetary Science Conference*, abstract #1826

1135 Hiraoka, K., Arakawa, M., Setoh, M., & Nakamura, A. M. (2008). Measurements of target compressive and
1136 tensile strengthfor application to impact cratering on ice-silicate mixtures. *Journal of Geophysical Research,*
1137 *113*, E02012. https://doi.org/10.1029/2007JE002926

Holsapple, K. A. (2009). On the "strength" of the small bodies of the solar system: A review of strength theories and their implementation for analyses of impact disruptions. *Planetary and Space Science, 57(2)*, 127-141. https://doi.org/10.1016/j.pss.2008.05.015

Hopkins, R. T., Osinski, G. R., & Collins, G. S. (2019). Formation of Complex Craters in Layered Targets with Material Anisotropy. *Journal of Geophysical Research: Planet, 124(2)*, 349-373. https://doi.org/10.1029/2018JE005819

Ivanov, B. A., Deniem, D., & Neukum, G. (1997). Implementation of dynamic strength models into 2D hydrocodes: Application for atmospheric breakup and impact cratering. *International Journal of Impact Engineering, 20*(1-5), 411-430. https://doi.org/10.1016/S0734-743X(97)87511-2

Ivanov, B. A., Melosh, H. J., & Pierazzo, E. (2010). Basin-forming impacts: Reconnaissance modeling. *Geological Society of America Special Papers 2010, 465*, 29-49. https://doi.org/10.1130/2010.2465(03)

Ivanov, B. A., & Pierazzo, E. (2011). Impact cratering in H_2O-bearing targets on Mars: Thermal field under craters as starting conditions for hydrothermal activity. *Meteoritics & Planetary Science, 46*(4), 601-619. https://doi.org/10.1111/j.1945-5100.2011.01177.x

Jaeger, J. C., Cook, N. G. W., & Zimmerman, R.W. (2007). *Fundamentals of Rock mechanics*. Backwell Publishing, 4th edition, 475 pp.

JeongAhn, Y., & Malhotra, R. (2015). The current impact flux on Mars and its seasonal variation. *Icarus, 262*, 140-153. https://doi.org/10.1016/j.icarus.2015.08.032

Johnson, W. E., & Anderson, C. E. (1987). History and application of hydrocodes in hypervelocity impact. *International Journal of Impact Engineering, 5(1-4)*, 423-439. https://doi.org/10.1016/0734-743X(87)90058-3

Jones, S. J. (1982). The confined compressive strength of polycrystalline ice. *Journal of Glaciology, 28*, 171-177. https://doi.org/10.3189/S0022143000011874

Jones, A.P., McEwen, A. S., Tornabene, L. L., Baker, V. R., Melosh, H. J., & Berman, D. C. (2011). A geomorphic analysis of Hale crater, Mars: The effects of impact into ice-rich crust. *Icarus, 211*(1), 259-272. https://doi.org/10.1016/j.icarus.2010.10.014

Kadish, S. J., Head, J. W., & Barlow, N. G. (2010). Pedestal crater heights on Mars: A proxy for the thicknesses of past, ice-rich, Amazonian deposit. *Icarus, 210(*1), 92-101. https://doi.org/10.1016/j.icarus.2010.06.021

Lange, M. A., & Ahrens, T. J. (1987), Impact experiments in low-temperature ice. *Icarus, 69(3)*, 506-518, https://doi.org/10.1016/0019-1035(87)90020-0

Lee, J. H., & Huang, T.J. (2014). Vehicle–snow interaction: Testing, modeling and validation for combined longitudinal and lateral slip. *Journal of Terramechanics, 55*, 1-16. https://doi.org/10.1016/j.jterra.2014.05.002.

Lundborg, N. (1968). Strength of rock-like materials. *International Journal of Rock Mechanics and Mining Science, 5*(5), 427-454. https://doi.org/10.1016/0148-9062(68)90046-6

Luther, R., Artemieva, N., Ivanova, M., Lorenz, C., & Wünnemann, K. (2017). Snow carrots after the Chelyabinsk event and model implications for highly porous solar system objects. *Meteoritics & Planetary Science, 52*(5), 979-999. https://doi.org/10.1111/maps.12831

Macke, R. J., Kiefer, W. S., Irving, A. J., & Britt, D. T. (2016). Density and Porosity measurements of Lunar and Martian Materials. 47th Lunar and Planetary Science Conference, #1294.

MacKinnon, D. J., & Tanaka, K. L. (1989), The impacted Martian crust: structure, hydrology, and some geologic implications. *Journal of Geophysical Research, 94*(10), 17359-17370. https://doi.org/10.1029/JB094iB12p17359

Madeleine, J.-B., Forget, F., Head, J. W., Levrard, B., Montmessin, F., & Millour, E. (2009). Amazonian northern mid-latitude glaciation on Mars: A proposed climate scenario. *Icarus, 203*(2), 390-405. https://doi.org/10.1016/j.icarus.2009.04.037

Mangold, N. (2005). High latitude patterned grounds on Mars: Classification, distribution and climatic control. *Icarus, 174*(2), 336-359. https://doi.org/10.1016/j.icarus.2004.07.030

Martellato, E., Vivaldi, V., Massironi, M., Cremonese, G., Marzari, F., Ninfo, A., & Haruyama, J. (2017). Is the Linné impact crater morphology influenced by the rheological layering on the Moon's surface? Insights from numerical modeling. *Meteoritics & Planetary Science, 52*(7), 1388-1411. https://doi.org/10.1111/maps.12892

McEwen, A.S., Banks, M. E., Baugh, N., Becker, K., Boyd, A., Bergstrom, J. W., et al. (2010). The High Resolution Imaging Science Experiment (HiRISE) during MRO's Primary Science Phase (PSP). *Icarus, 205*(1), 2-37. https://doi.org/10.1016/j.icarus.2009.04.023

McSween, H. Y., Taylor, G..J., & Wyatt, M. B. (2009), Elemental composition of the Martial Crust. *Science, 324*(5928), 736-739. https://doi.org/10.1126/science.1165871

Mellon, M.T., Jakosky, B. M., & Postawko, S. E. (1997), The persistence of equatorial ground ice on Mars. *Journal of Geophysical Research, 102*(E8), 19357-19370. https://doi.org/10.1029/97JE01346

Mellon, M.T., Boyton, W. V., Feldman, W. C., Arvidson, R. E., Titus, T. N., Bandfield, J. L., et al. (2008). A prelanding assessment of the ice table depth and ground ice characteristics in Martian permafrost at the Phoenix landing site. *Journal of Geophysical Research, 113*(E12), E00A25. https://doi.org/10.1029/2007JE003067

Mellon, M.T., Arvidson, R. E., Sizemore, H. G., Searls, M. L., Blaney, D. L., Cull, S., et al. (2009). Ground ice at the Phoenix Landing Site: Stability state and origin. *Journal of Geophysical Research, 114*(53), E00E07. https://doi.org/10.1029/2009JE003417

Melosh, H. J. (1979). Acoustic fluidization: A new geologic process?. *Journal of Geophysical Research: Solid Earth, 84*, 7513-7520. https://doi.org/10.1029/JB084iB13p07513

Melosh, H. J. (1989). *Impact cratering: A geologic process*. New York: Oxford University Press. 245 p.

Melosh, H. J., Ryan, E. V., & Asphaug, E. (1992). Dynamic Fragmentation in Impact: Hydrocode Simulation of Laboratory Impacts. *Journal of Geophysical Research, 97*(E9), 14,735-14,759. https://doi.org/10.1029/92JE01632

Melosh, H. J., & Ivanov, B. A. (1999). Impact crater collapse. *Annual Review of Earth and Planetary Science, 27*, 385-415. https://doi.org/10.1146/annurev.earth.27.1.385

Nunes, D. C., Smrekar, S. E., Fisher, B., Plaut, J. J., Holt, J. W., Head, J. W., et al. (2011). Shallow Radar (SHARAD), pedestal craters, and the lost Martian layers: Initial assessments. *Journal of Geophysical Research, 116*(E4), E04006. https://doi.org/10.1029/2010JE003690

Oberbeck, V. R., & Quaide, W. L. (1967). Estimated thickness of a fragmental surface layer of Oceanus Procellarum. *Journal of Geophysical Research, 72*(18), 4697-4704. https://doi.org/10.1029/JZ072i018p04697

O'Keefe, J. D., & Ahrens, T. J. (1982), Cometary and meteorite swarm impact on planetary surfaces. *Journal of Geophysical Research: Solid Earth, 87*(B8), 6668-6680. https://doi.org/10.1029/JB087iB08p06668

O'Keefe, J. D., Stewart, S. T., Lainhart, M. E., & Ahrens, T. J. (2001). Damage and rock-volatile mixture effects on impact crater formation. *International Journal of Impact Engineering, 26*, 543-553. https://doi.org/10.1016/S0734-743X(01)00112-9

Ono, T., Kumamoto, A., Nakagawa, H., Yamaguchi, Y., Oshigami, S., Yamaji, A., Kobayashi, T., Kasahara, Y., & Oya, H. (2009). Lunar Radar Sounder observations of subsurface layers under the nearside maria of the Moon. *Science, 323*, 909-912. https://doi.org/10.1126/science.1165988

Örmo, J., Rossi, A. P., & Housen, K. R. (2013). A new method to determine the direction of impact: Asymmetry of concentric impact craters as observed in the field (Lockne), on Mars, in experiments, and simulations. *Meteoritics & Planetary Science, 48*(3), 403-419. https://doi.org/10.1111/maps.12065

Osinski, G.R., Silber, E. A., Clayton, J., Grieve, R. A. F., Hansen, K., Johnson, C. L., Kalynn, J., & Tornabene, L.L. (2019). Transitional impact craters on the Moon: Insight into the effect of target lithology on the impact cratering process. *Meteoritics & Planetary Science, 54(3)*, 573-591. https://doi.org/10.1111/maps.13226

Pathare, A. V., Feldman, W. C., Prettyman, T. H., and Maurice, S. (2018). Driven by excess? Climatic implications of new global mapping of near-surface water-equivalent hydrogen on Mars. *Icarus, 301*, 97-116. https://doi.org/10.1016/j.icarus.2017.09.031

Petrovic, J. J. (2003). Review Mechanical properties of ice and snow. *Journal of Material Sciences, 38*, 1-6. https://doi.org/10.1023/A:1021134128038

Pierazzo, E., Vickery, A. M., & Melosh, H. J. (1997). A Reevaluation of Impact Melt Production. *Icarus, 127*, 408-423. https://doi.org/10.1006/icar.1997.5713

Pierazzo, E., Artemieva, N., & Ivanov, B. A. (2005). Starting conditions for hydrothermal systems underneath Martian craters: Hydrocode modeling. In T. Kenkmann, F. Hörz & A. Deutsch (Eds.), *Large meteorite impacts III* (443-457), Geological Society of America Special Paper, 384. https://doi.org/10.1130/0-8137-2384-1.443

Pierazzo E., Artemieva, N., Asphaug, E., Baldwin, E. C., Cazamias, J., Coker, R., et al. (2008). Validation of numerical codes for impact and explosion cratering: Impacts on strengthless and metal targets. *Meteoritics & Planetary Science, 43*(12), 1917-1938. https://doi.org/10.1111/j.1945-5100.2008.tb00653.x

Prieur, N. C., Rolf, T., Wünnemann, K., & Werner, S. C., (2018). Formation of Simple Impact Craters in Layered Targets: Implications for Lunar Crater Morphology and Regolith Thickness. *Journal of Geophysical Research: Planets, 123(6)*, 1555-1578. https://doi.org/10.1029/2017JE005463

Quaide, W. L., & Oberbeck, V. R. (1968). Thickness Determinations of the Lunar Surface Layer from Lunar Impact Craters. *Journal and Geophysical Research, 73(16)*, 5247-5270. https://doi.org/10.1029/JB073i016p05247

Robbins, S. J., & Hynek, B. M. (2012). A new global database of Mars impact craters ≥1 km: 1. Database creation, properties, and parameters. *Journal of Geophysical Research, 117*(E5), E05004. https://doi.org/10.1029/2011JE003966

Robinson, M. S., Ashley, J. W., Boyd, A. K., Wagner, R. V., Speyerer, E. J., Hawke, B. R., Hiesinger, H., & van der Bogert, C. H. (2012). Confirmation of sublunear voids and thin layering in mare deposits. *Planetary and Space Science, 69*,18-27. https://doi.org/10.1016/j.pss.2012.05.008

Schmidt, R. M., & Housen, K. R. (1987). Some recent advances in the scaling of impact and explosion cratering. *International Journal of Impact Engineering, 4(1-4)*, 543-560. https://doi.org/10.1016/0734-743X(87)90069-8

Schulson, E. M. (1990). The brittle compressive fracture of ice. *Acta Metallurgica et Materialia, 38(10)*, 1963-1976. https://doi.org/10.1016/0956-7151(90)90308-4

Schulson, E. M. (2001). Brittle failure of ice. *Engineering of Fracture Mechanics, 68(17-18)*, 1839-1887. https://doi.org/10.1016/S0013-7944(01)00037-6

Senft, L. E., & Stewart, S. T. (2007). Modeling impact cratering in layered surfaces. *Journal of Geophysical Research, 112(E11)*, E11002. https://doi.org/2007JGRE..11211002S

Senft, L. E., & Stewart, S. T. (2008). Impact crater formation in icy layered terrains on Mars. *Meteoritics & Planetary Science, 43*(12), 1993-2013. https://doi.org/10.1111/j.1945-5100.2008.tb00657.x

Shoemaker, E. M. (1962). Interpretation of lunar craters. In: *Physics and Astronomy of the Moon*, edited by Kopal Z., New York, Academic, pp. 283-359.

Silber, E. A., & Johnson, B. C. (2017). Impact crater morphology and the structure of Europa's ice shell. *Journal of Geophysical Research: Planets, 122*, 2685-2701. https://doi.org/10.1002/2017JE005456

Silber, E. A., Osinski, G. R., Johnson, B. C., & Grieve, R. A. F. (2017). Effect of impact velocity and acoustic fluidization on the simple-to-complex transition of lunar craters. *Journal of Geophysical Research: Planets, 122*, 800-821. https://doi.org/10.1002/2016JE005236

Steel, D. (1998), Distributions and Moments of Asteroid and Comet Impact Speeds upon the Earth and Mars. *Planetary and Space Science, 46*, 473–478. https://doi.org/10.1016/S0032-0633(97)00232-8

Stuurman, C. M., Osinski, G. R., Holt, J. W., Levy, J. S., Brothers, T. C., Kerrigan, M., & Campbell, B. A. (2016). SHARAD detection and characterization of subsurface water ice deposits in Utopia Planitia, Mars. *Geophysical Research Letters, 43*(18), 9484-9491. https://doi.org/10.1002/2016GL070138

Thompson, S. L. (1970). *Improvements in the CHART–D radiation hydrodynamic code I: Analytical equation of state*. Sandia National Laboratories, Report SC–RR–70–28.

Thompson, S. L., & Lauson, H. S. (1972). *Improvements in the CHART–D radiation-hydrodynamic code III: Revised analytical equation of state*. Sandia National Laboratories, Report SC–RR–710714.

Tillotson, J. H. (1962). *Metallic equations of state for hypervelocity impact*. General Atomic, Report GA–3216.

Ulaby, F. T., Moore, R. K., & Fung, A. K. (1986). *Microwave Remote Sensing: Active and passive. Volume 3 - From theory to applications*. Norwood, MA: Artech House.

Vasconcelos, M. A. R., Rocha, F. F., Crósta, A. P., Wünnemann, K., Güldemeister, N., Leite, E. P, Ferreira, J. C., & Reimold, W. U. (2019). Insights about the formation of a complex impact structure formed in basalt from numerical modeling: The Vista Alegre structure, southern Brazil. *Meteoritics & Planetary Science, 54(10)*, 2373-2383. https://doi.org/10.1111/maps.13298

Viola, D., McEwen, A. S., Dundas, C. M., & Byrne, S. (2015). Expanded secondary craters in the Arcadia Planitia region Mars: Evidence for tens of Myr-old shallow subsurface ice. *Icarus, 248*, 190-204. https://doi.org/10.1016/j.icarus.2014.10.032

Warner, N. H., Golombek, M. P., Sweeney, J., Fergason, R., Kirk, R., & Schwartz, C. (2017). Near Surface Stratigraphy and Regolith Production in Southwestern Elysium Planitia, Mars: Implications for Hesperian-Amazonian Terrains and the InSight Lander Mission. *Space Science Reviews, 211*(1-4), 147-190. https://doi.org/10.1007/s11214-017-0352-x

Watters, W. A., Geiger, L. M., Fendrock, M., & Gibson, R. (2015). Morphometry of small recent impact craters on Mars: Size and terrain dependence, short-term modification. *Journal of Geophysical Research: Planets, 120*, 226-254. https://doi.org/10.1002/2014JE004630

Watters, W. A., Hundal, C. B., Radford, A., Collins, G. S., & Tornabene, L. L. (2017). Dependence of secondary crater characteristics on downrange distance: High-resolution morphometry and simulations. *Journal of Geophysical Research: Planets, 122*, 1773-1800. https://doi.org/10.1002/2017JE005295

Weider, S. Z., Crawford, I. A., & Joy, K. H. (2010). Individual lava flow thicknesses in Oceanus Procellarum and Mare Serenitatis determined from Clementine multispectral data. *Icarus, 209*, 323-336. https://doi.org/10.1016/j.icarus.2010.05.010

Weiss, J., & Schulson, E. M. (1995). The failure of fresh-water granular ice under multi-axial compressive loading. *Acta Metallurgica et Materialia, 43*, 2303-2315. https://doi.org/10.1016/0956-7151(94)00421-8

Wieczorek, M. A., Neumann, G. A., Nimmo, F., Kiefer, W. S., Taylor, G. J., Melosh, H. J., et al. (2013). The crust of the Moon as seen by GRAIL. *Science, 339*(6120), 671-675. https://doi.org/10.1126/science.1231530

Wünnemann, K., & Ivanov, B. A. (2003). Numerical modelling of the impact crater depth-diameter dependence in an acoustically fluidized target. *Planetary and Space Science, 51*, 831-845. https://doi.org/10.1016/j.pss.2003.08.001

Wünnemann, K., Collins, G. S., & Melosh, H. J. (2006). A strain–based porosity model for use in hydrocode simulations of impacts and implications for transient crater growth in porous targets. *Icarus, 180*(2), 514-527. https://doi.org/10.1016/j.icarus.2005.10.013

Wünnemann, K., Collins, G. S., & Osinski, G. R. (2008). Numerical modelling of impact melt production in porous rock. *Earth and Planetary Science Letters, 269*(3-4), 530-539. https://doi.org/10.1016/j.epsl.2008.03.007

Zuber, M.T., Smith, D. E., Watkins, M. M., Asmar, S. W., Konopliv, A. S., Lemoine, F. G., et al. (2013). Gravity Field of the Moon from the Gravity Recovery and Interior Laboratory (GRAIL) Mission. *Science, 339*(6120), 668-671. https://doi.org/10.1126/science.1231507

Table 1. Numerical model parameters (cf. section 3.3 for details on the adopted values).

Symbol	Definition	*Crater 1*	*Crater 2*
GRID:		448×416	590×550
R	Projectile Radius	20 m	15 m
v_i	Impact Velocity	7 (5) km/s	
	Material	basalt	
ρ_i	Material Density	2.86 kg/m^3	
	Material Porosity	10%	
TARGET: Porous ice			
Y_d	Damaged cohesion	10 kPa	
μ_d	Coefficient of friction (damaged material)	0.18	
Y_M	Von Mises plastic limit for damaged material	0.11 GPa	
T_m	Melt Temperature	273 K	
	Porosity	35%	
	Non-porous ice		
Y_0	Cohesion (yield strength at zero pressure)	50 kPa	
μ_i	Coefficient of internal friction	2.0	
Y_d	Damaged cohesion	10 kPa	
μ_d	Coefficient of friction (damaged material)	0.18	
Y_M	Von Mises plastic limit	0.11 GPa	
T_m	Melt Temperature	273 K	
	Basalt crust		
Y_0	Cohesion (yield strength at zero pressure)	20 MPa	
μ_i	Coefficient of internal friction	1.4	
Y_d	Damaged cohesion	0.2 MPa	
μ_d	Coefficient of friction (damaged material)	0.84	
Y_M	Von Mises plastic limit	3.5 GPa	
T_m	Melt Temperature	1360 K	
	Porosity	10%	

Figure 1.

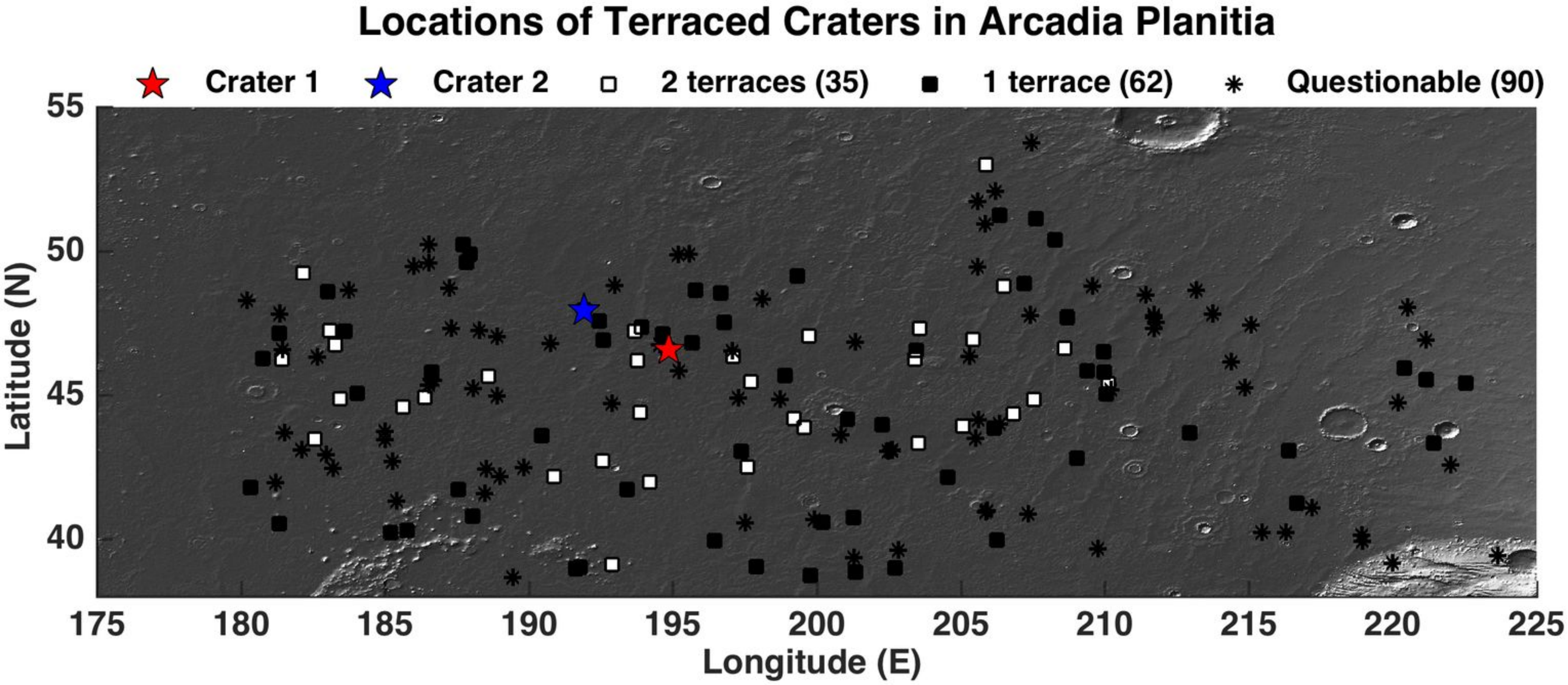
Locations of Terraced Craters in Arcadia Planitia
Crater 1
Crater 2
2 terraces (35)
1 terrace (62)
Questionable (90)
55
50
45
40
Latitude (N)
175
180
185
190
195
200
205
210
215
220
225
Longitude (E)

Figure 2.

A

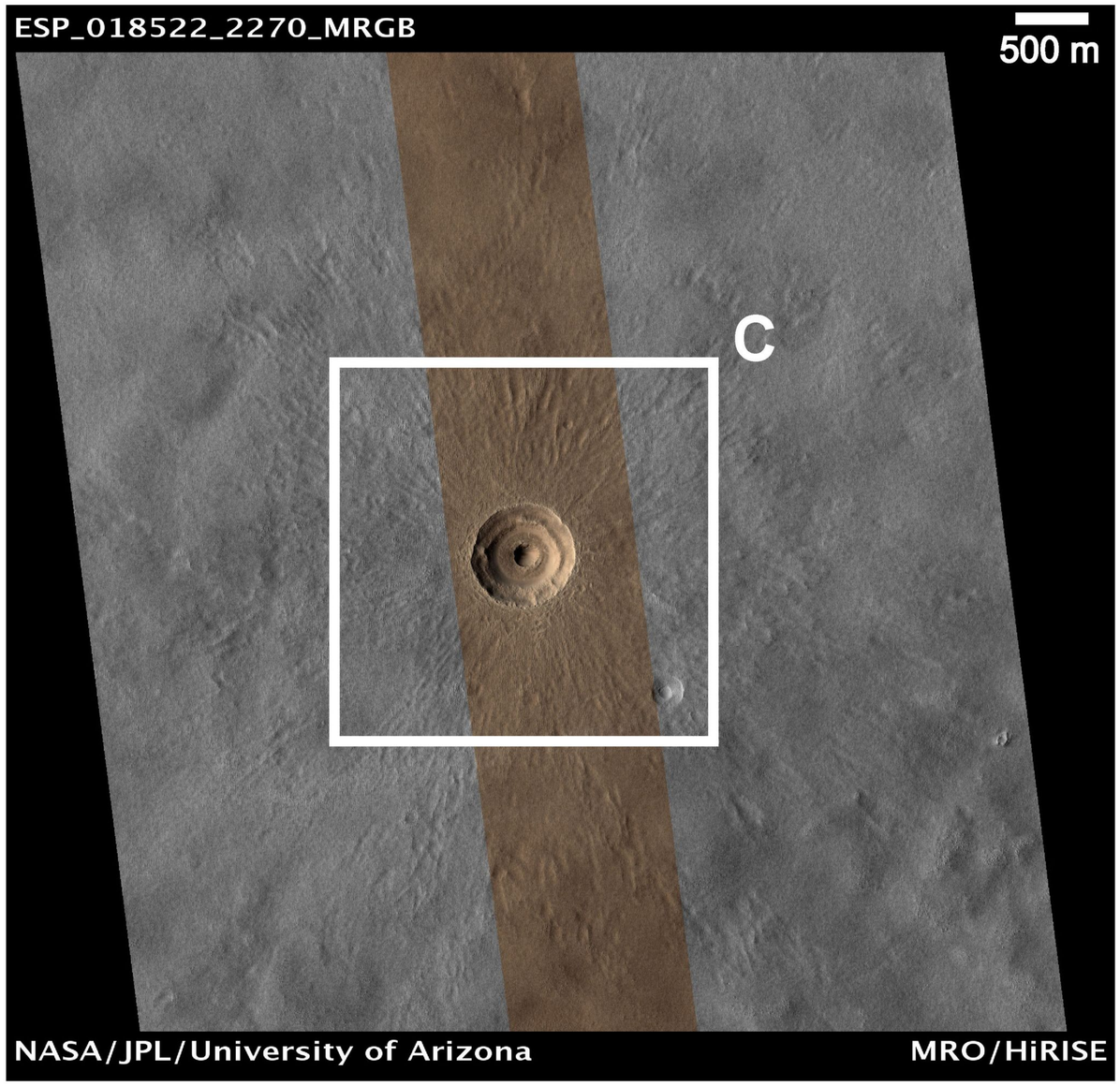
ESP_018522_2270_MRGB
500 m
C
NASA/JPL/University of Arizona
MRO/HiRISE

B

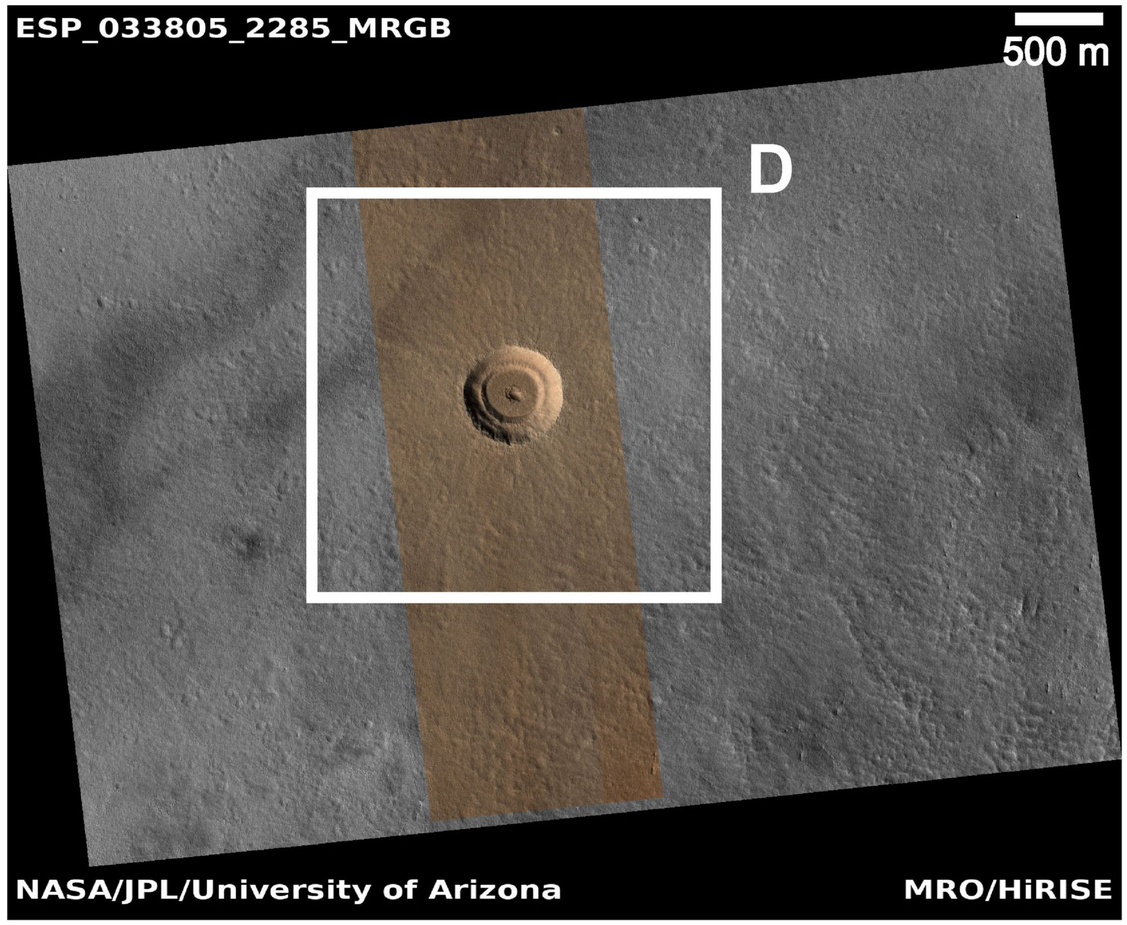
ESP_033805_2285_MRGB
500 m
D
NASA/JPL/University of Arizona
MRO/HiRISE

C

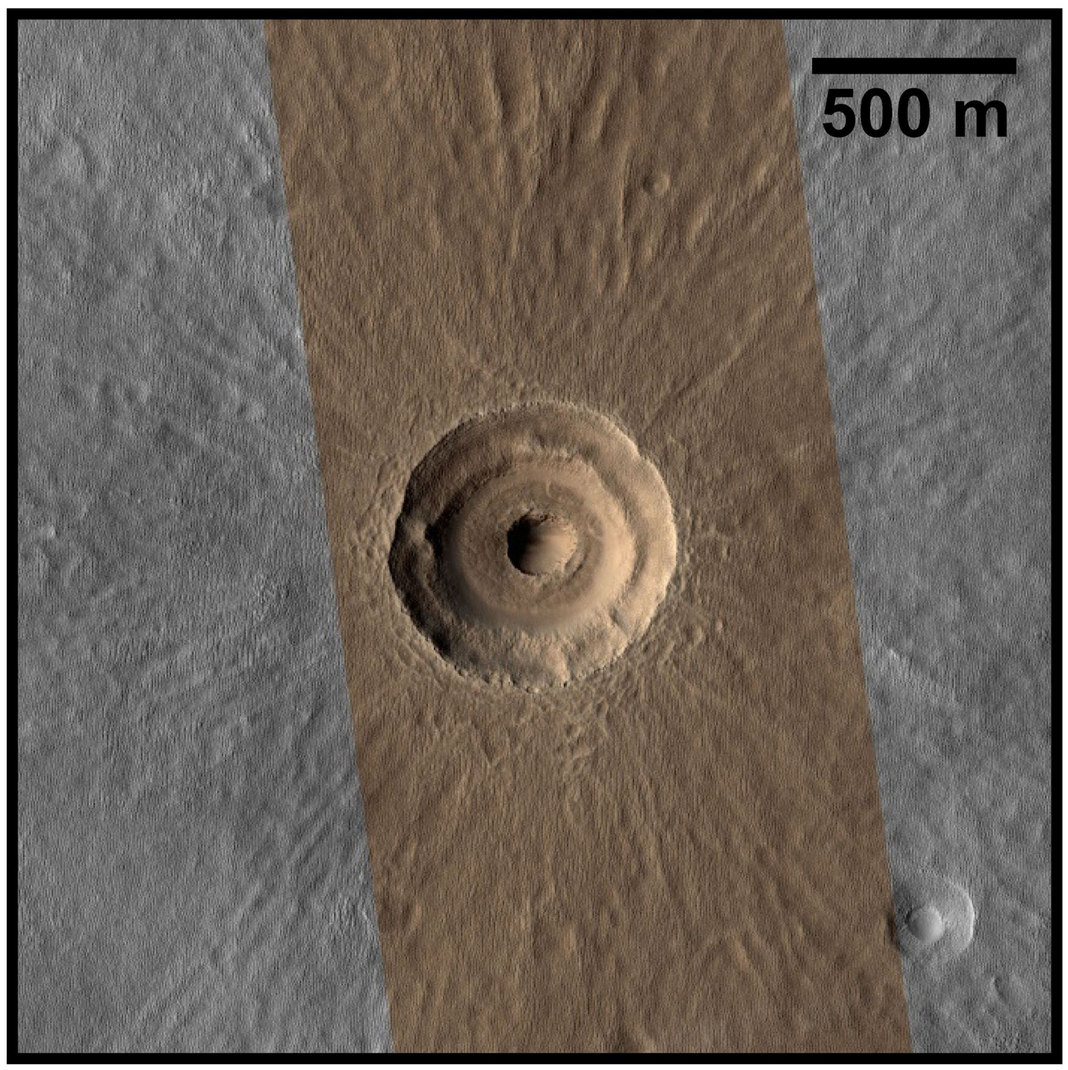
500 m

D

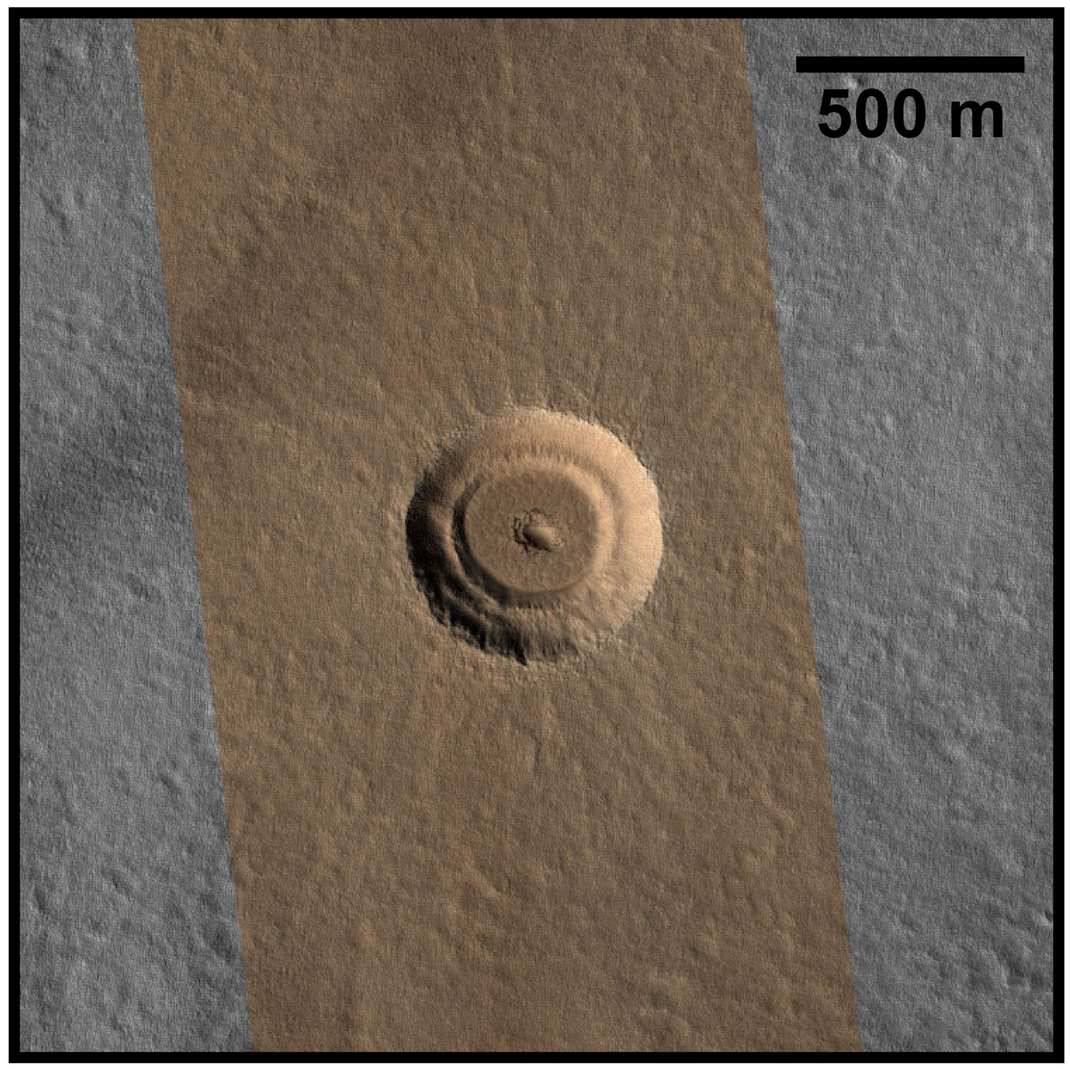
500 m

Figure 3.

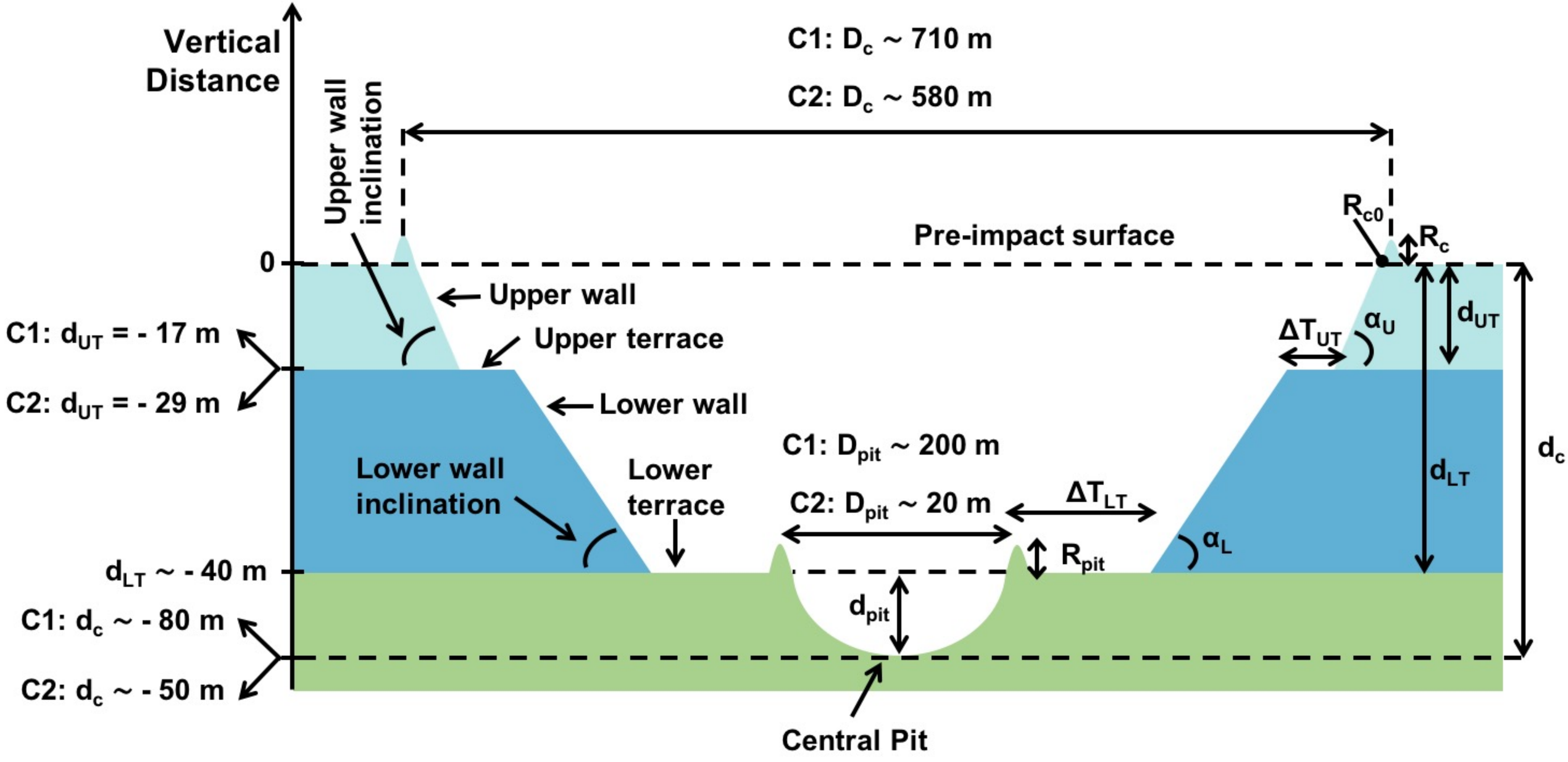
Vertical Distance
C1: D_c ~ 710 m
C2: D_c ~ 580 m
Upper wall inclination
R_{c0}
R_c
Pre-impact surface
0
Upper wall
Upper terrace
Lower wall
C1: d_{UT} = - 17 m
C2: d_{UT} = - 29 m
ΔT_{UT}
α_U
d_{UT}
C1: D_{pit} ~ 200 m
Lower wall inclination
Lower terrace
C2: D_{pit} ~ 20 m
ΔT_{LT}
R_{pit}
α_L
d_{LT}
d_c
d_{LT} ~ - 40 m
d_{pit}
C1: d_c ~ - 80 m
C2: d_c ~ - 50 m
Central Pit

Figure 4.

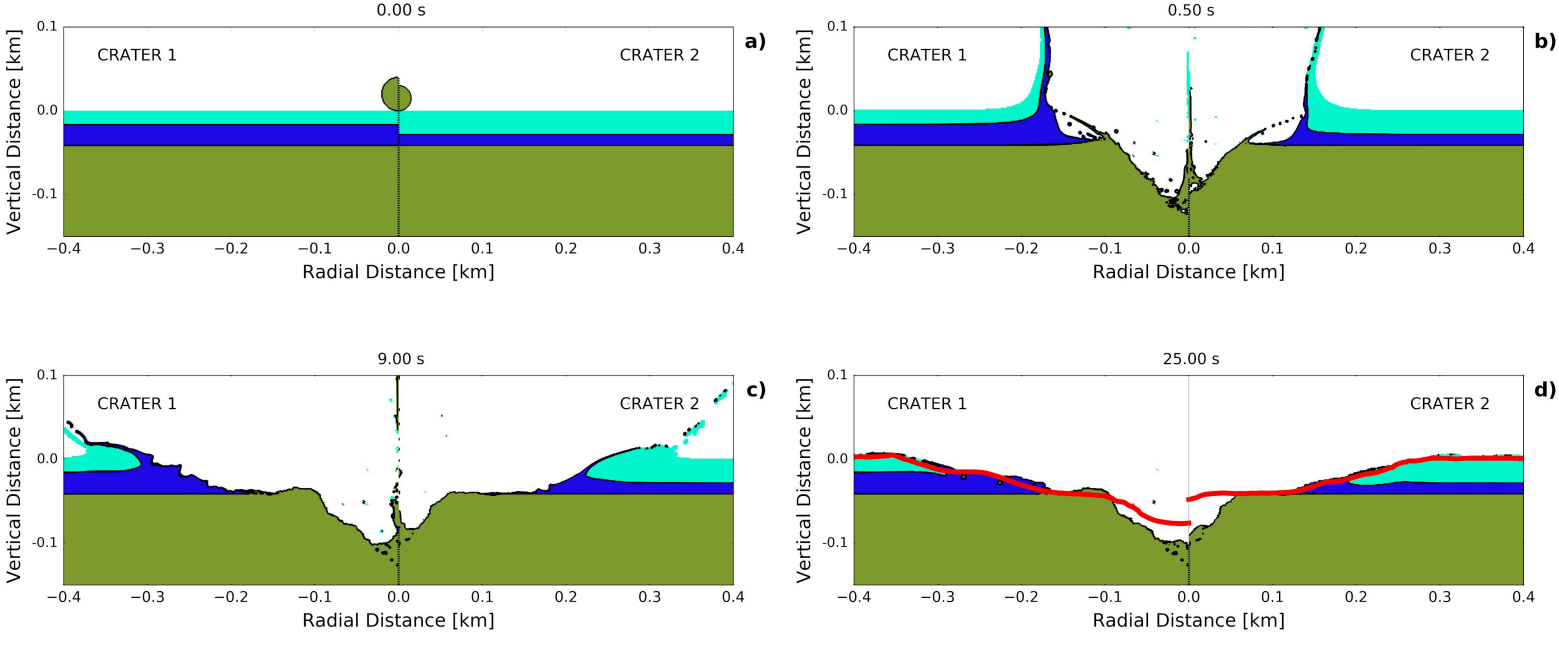
0.00 s
CRATER 1
CRATER 2
a)
0.50 s
b)
9.00 s
c)
25.00 s
d)
Vertical Distance [km]
Radial Distance [km]
0.1
0.0
-0.1
−0.4
−0.3
−0.2
−0.1
0.0
0.1
0.2
0.3
0.4

Figure 5.

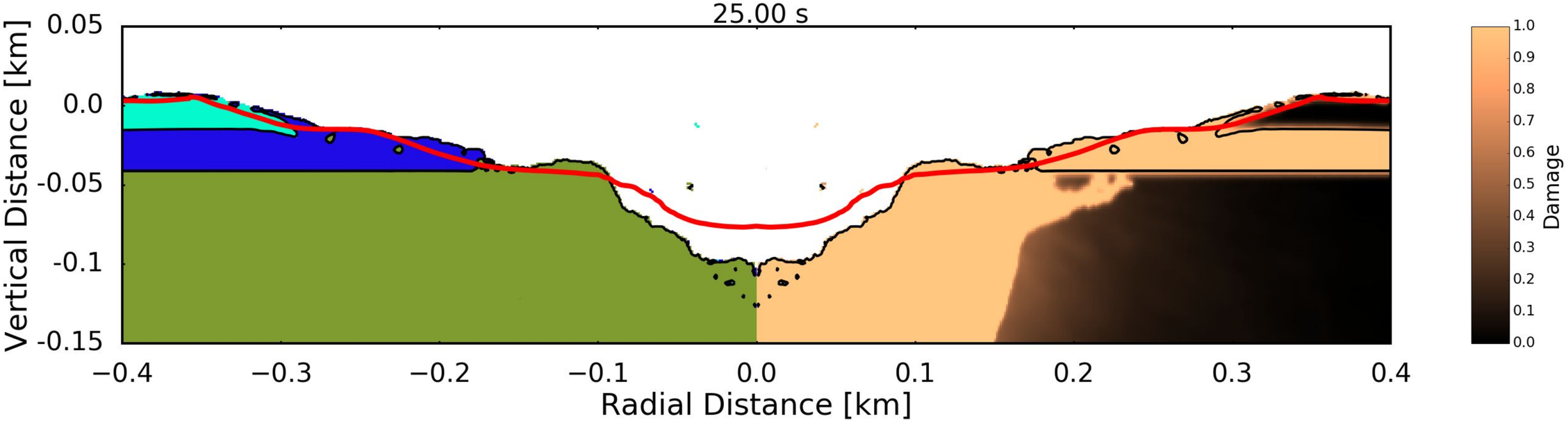
25.00 s
Vertical Distance [km]
0.05
0.0
-0.05
-0.1
-0.15
−0.4
−0.3
−0.2
−0.1
0.0
0.1
0.2
0.3
0.4
Radial Distance [km]
Damage
1.0
0.9
0.8
0.7
0.6
0.5
0.4
0.3
0.2
0.1
0.0

Figure 6.

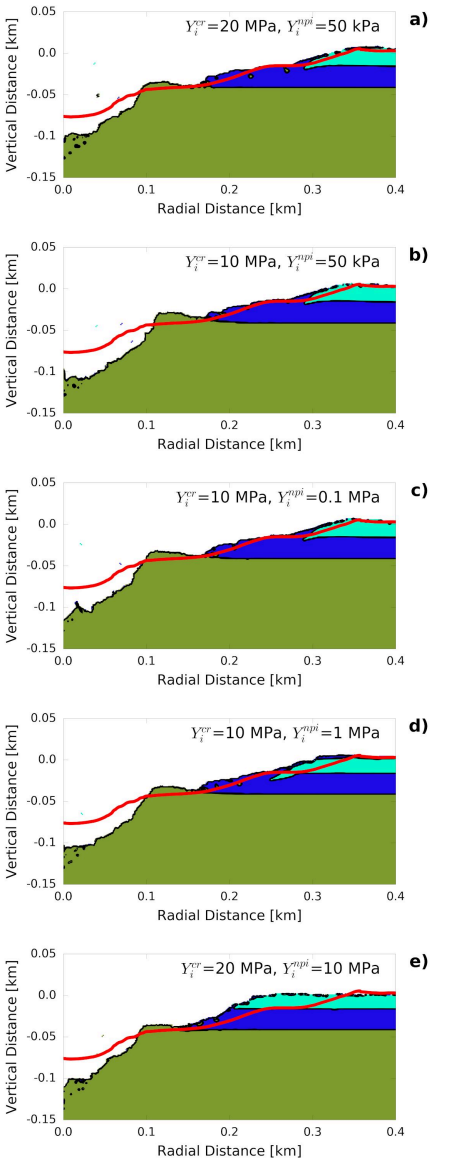
a)
Y_i^{cr}=20 MPa, Y_i^{npi}=50 kPa
b)
Y_i^{cr}=10 MPa, Y_i^{npi}=50 kPa
c)
Y_i^{cr}=10 MPa, Y_i^{npi}=0.1 MPa
d)
Y_i^{cr}=10 MPa, Y_i^{npi}=1 MPa
e)
Y_i^{cr}=20 MPa, Y_i^{npi}=10 MPa
Vertical Distance [km]
Radial Distance [km]
0.05
0.0
-0.05
-0.1
-0.15
0.1
0.2
0.3
0.4

Figure 7.

a)

Depth-to-Diameter ratio

2.50
2.25
2.00
1.75
1.50
1.25
1.00

b)

Diameter

1.00
0.75
0.50

c)

Depth

2.25
2.00
1.75
1.50
1.25
1.00

0.01
0.10
1.00
10.00

Yi

Figure 8.

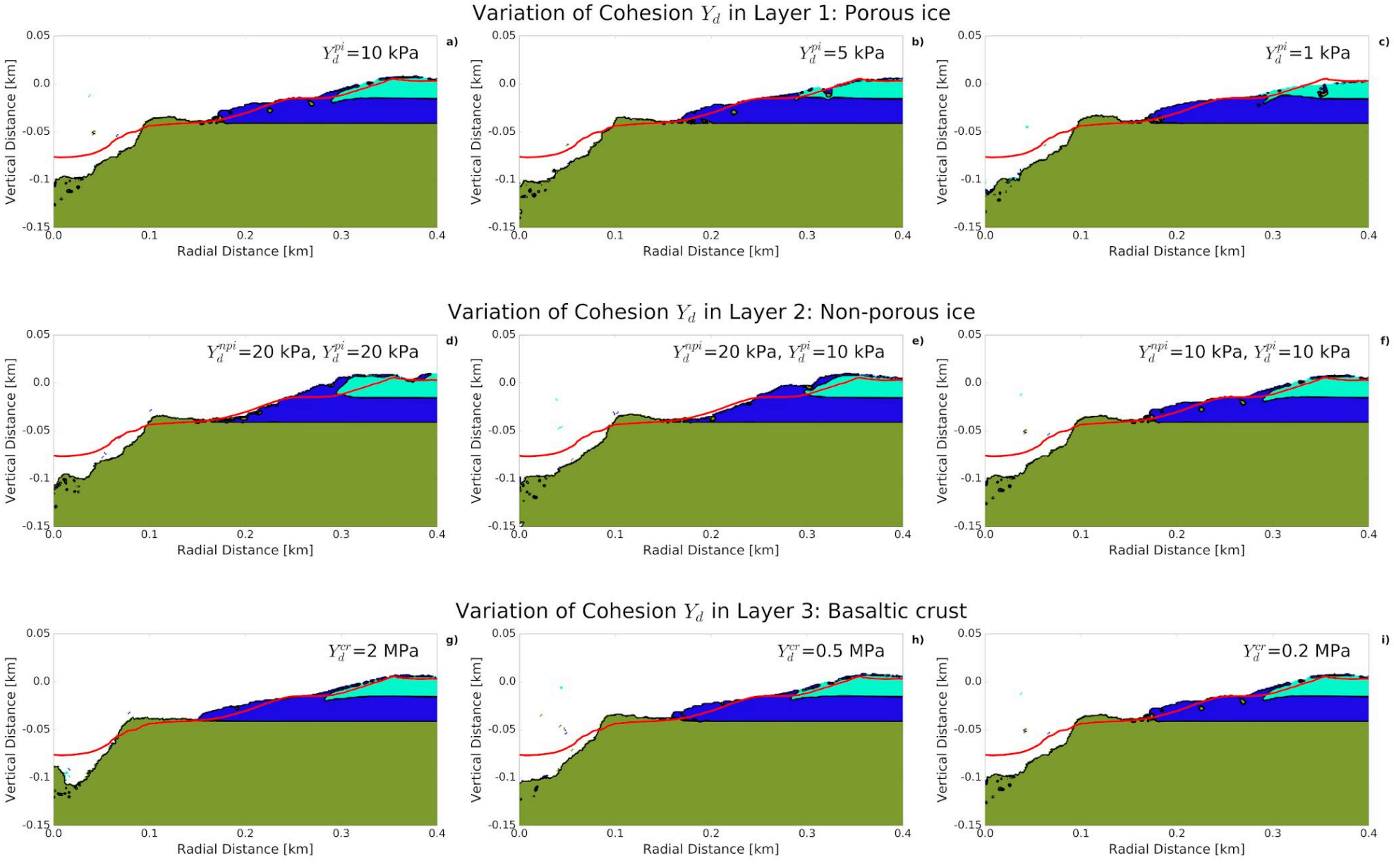
Variation of Cohesion Y_d in Layer 1: Porous ice
Y_d^{pi}=10 kPa
a)
Y_d^{pi}=5 kPa
b)
Y_d^{pi}=1 kPa
c)
Variation of Cohesion Y_d in Layer 2: Non-porous ice
Y_d^{npi}=20 kPa, Y_d^{pi}=20 kPa
d)
Y_d^{npi}=20 kPa, Y_d^{pi}=10 kPa
e)
Y_d^{npi}=10 kPa, Y_d^{pi}=10 kPa
f)
Variation of Cohesion Y_d in Layer 3: Basaltic crust
Y_d^{cr}=2 MPa
g)
Y_d^{cr}=0.5 MPa
h)
Y_d^{cr}=0.2 MPa
i)
Vertical Distance [km]
Radial Distance [km]
0.05
0.0
-0.05
-0.1
-0.15
0.0
0.1
0.2
0.3
0.4

Figure 9.

a)

Depth−to−Diameter ratio

2.5

2.0

1.5

1.0

b)

Diameter

1.00

0.75

c)

Depth

2.00

1.75

1.50

1.25

1.00

0.001

0.010

0.100

1.000

10.000

Yi

Figure 10.

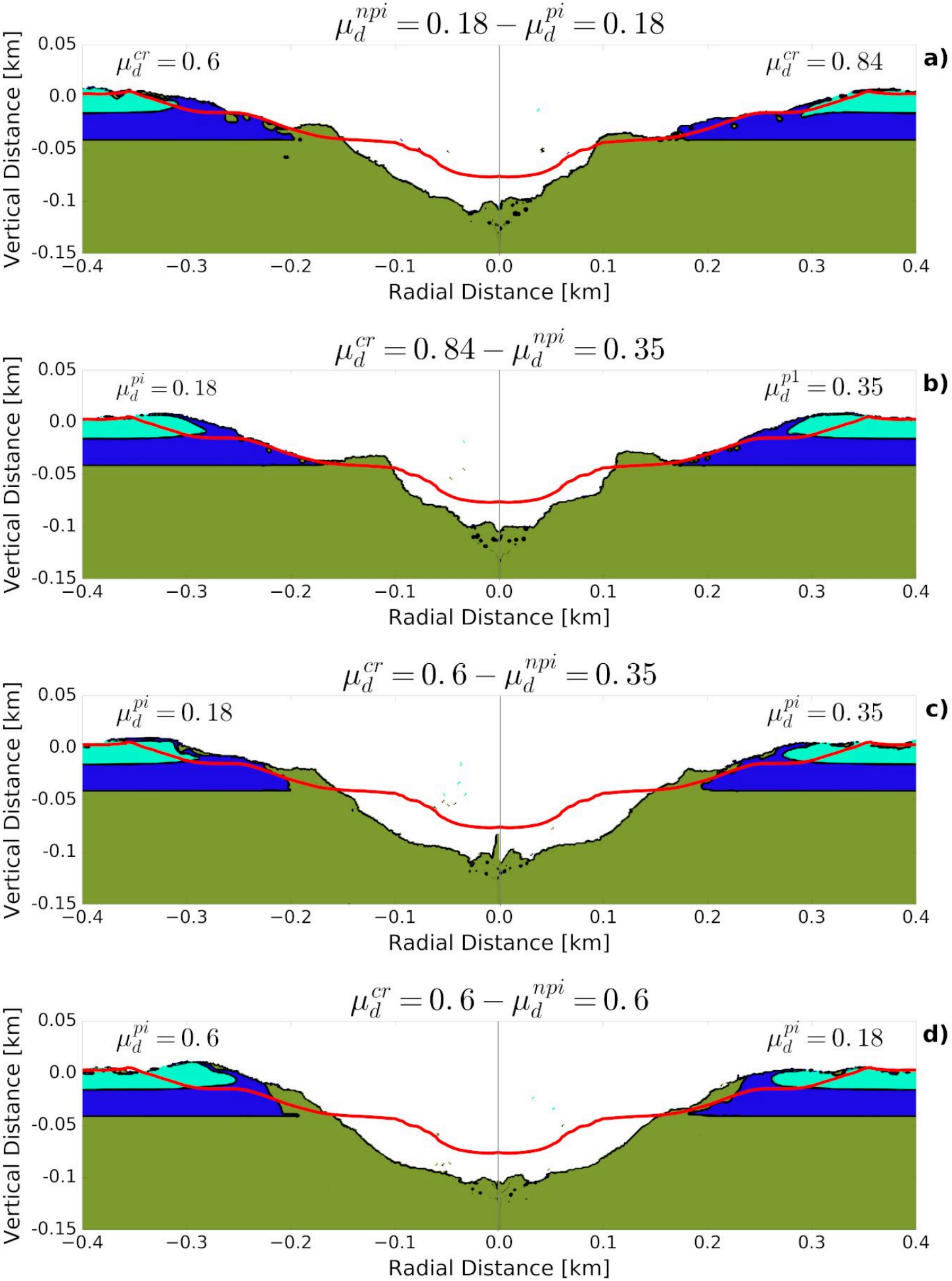
$\mu_d^{npi} = 0.18 - \mu_d^{pi} = 0.18$
$\mu_d^{cr} = 0.6$
$\mu_d^{cr} = 0.84$
a)
$\mu_d^{cr} = 0.84 - \mu_d^{npi} = 0.35$
$\mu_d^{pi} = 0.18$
$\mu_d^{pl} = 0.35$
b)
$\mu_d^{cr} = 0.6 - \mu_d^{npi} = 0.35$
$\mu_d^{pi} = 0.18$
$\mu_d^{pi} = 0.35$
c)
$\mu_d^{cr} = 0.6 - \mu_d^{npi} = 0.6$
$\mu_d^{pi} = 0.6$
$\mu_d^{pi} = 0.18$
d)
Vertical Distance [km]
Radial Distance [km]
0.05
0.0
-0.05
-0.1
-0.15
−0.4
−0.3
−0.2
−0.1
0.0
0.1
0.2
0.3
0.4

Figure 11.

a)

Depth−to−Diameter ratio

2.00
1.75
1.50
1.25
1.00

b)

Diameter

1.50
1.25
1.00
0.75

c)

Depth

2.50
2.25
2.00
1.75
1.50

0.1
0.2
0.3
0.4
0.5
0.6
0.7

ud

Figure 12.

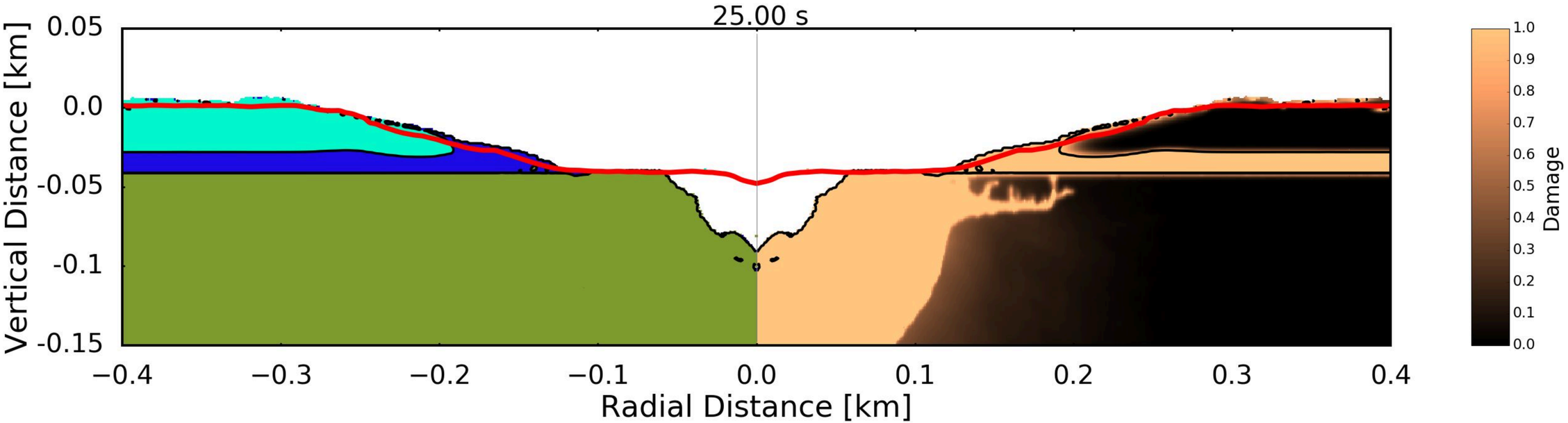
25.00 s
Vertical Distance [km]
0.05
0.0
-0.05
-0.1
-0.15
−0.4
−0.3
−0.2
−0.1
0.0
0.1
0.2
0.3
0.4
Radial Distance [km]
Damage
1.0
0.9
0.8
0.7
0.6
0.5
0.4
0.3
0.2
0.1
0.0

Figure 13.

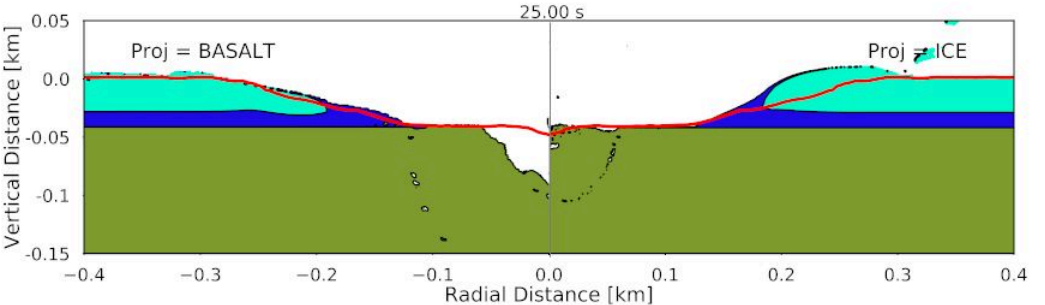
25.00 s
Proj = BASALT
Proj = ICE
Vertical Distance [km]
0.05
0.0
-0.05
-0.1
-0.15
−0.4
−0.3
−0.2
−0.1
0.0
0.1
0.2
0.3
0.4
Radial Distance [km]